Materials & Design 206 (2021) 109794

Contents lists available at ScienceDirect

Materials & Design

journal homepage: www.elsevier.com/locate/matdes

Grain-orientation induced stress formation in AA2024 monocrystal and bicrystal using Crystal Plasticity Finite Element Method

Qi Zhao [a,c], Magd Abdel Wahab [b,c,*], Yong Ling [c], Zhiyi Liu [d]

[a] School of Materials Science and Engineering, Hubei University of Automotive Technology, Shiyan 442002, PR China
[b] CIRTech Institute, Ho Chi Minh City University of Technology (HUTECH), Ho Chi Minh City, Viet Nam
[c] Soete Laboratory, Faculty of Engineering and Architecture, Ghent University, Technologiepark Zwijnaarde 903, B-9052 Zwijnaarde, Belgium
[d] School of Materials Science and Engineering, Central South University, Changsha 410083, PR China

HIGHLIGHTS

- Grain orientation effect on stress formation essentially attributes to the difference in Schmid Factors of slip systems.
- No certain relationship exists between monocrystal stress formation and GB stress at bicrystal model.
- Goss and Cube are the best two ones for relieving GB stress concentration.
- The contribution from 5-independent slip system criterion needs to be considered at GB interaction.

GRAPHICAL ABSTRACT

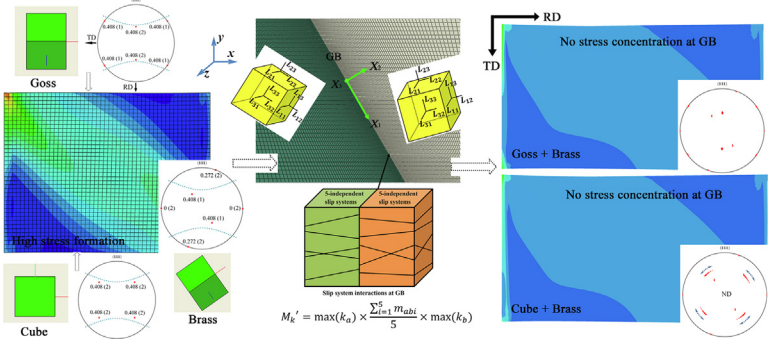

ARTICLE INFO

Article history:
Received 17 March 2021
Revised 16 April 2021
Accepted 2 May 2021
Available online 6 May 2021

Keywords:
AA2024 alloy
Goss orientation
Grain boundary
Crystal plasticity
Finite element method
Dislocation interaction

ABSTRACT

Stress formation of monocrystals and bicrystals is investigated in specific oriented grains and grain boundaries of AA2024 alloy by using Crystal Plasticity Finite Element Method (CPFEM). The simulations show that the maximum Schmid factor (SF) value and the number of equivalent initial slip system (EISS) play a principal role in controlling the magnitude of internal stress within monocrystals. For bicrystal model, Goss and Cube grains are not the best ones for relieving stress concentration caused by their orientations, but they are the best ones for relieving grain boundary (GB) stress concentration. To this end, the dependence relations are discussed between GB stress and an advanced comprehensive factor combining SF, and geometry compatibility factor for 5 independent slip systems. It is found that this proposed comprehensive factor considering the contribution from 5 to independent slip systems effectively improves its dependence on GB stress.

1. Introduction

From the aspect of texture effect on fatigue resistance of Al-Cu-Mg alloy, grain boundary (GB) character and stress formation induced by grain orientation are two important factors that exert great influence on fatigue resistance. Recently, Liu and Li et al. [1–3] revealed that due to the large twist angle boundary between Goss grain and other oriented grains, Goss grains were thereby able to facilitate crack deflection. Interestingly, it was also observed that even with large twist angle between Brass and other oriented grains, Brass grain still showed little resistance to crack propagation during fatigue test. This phenomenon uncovers that the fatigue resistance is also closely related to the stress formation

* Corresponding author at: CIRTech Institute, Ho Chi Minh City University of Technology (HUTECH), Ho Chi Minh City, Viet Nam.
E-mail addresses: magd.a.w@hutech.edu.vn, magd.abdelwahab@UGent.be (M. Abdel Wahab).

https://doi.org/10.1016/j.matdes.2021.109794
0264-1275/

and distribution that could be caused by different grain orientations. To the best of our knowledge, due to the orientation difference in each grain, the resolved shear stress would be different as well, which would result in different plastic slip and stress evolution in each crystal, and stress concentration at GBs. It was reported in Ref. [1] that the bad fatigue resistance for Brass was principally contributed to the high stress formation within Brass grains. This makes Brass grains having poor capability in relieving stress concentration caused by cycle loading. Besides, high stress is usually formed at GBs that often are regarded as original sites for fatigue cracks. Bieler et al. [4] found by experimental methods that "good" vs. "bad" GBs were often invoked as the significant reasons for critical damage nucleation. In essence, GB is considered as a bridge that connects neighboring grains. Even though GBs are often regarded as a barrier that could block dislocation movements, this blocking effects only occur at the initial stages of plastic deformation. When the microtraction reaches a yield threshold for GB, dislocation slipping in one grain could run through this GB to interact with another grain [5]. How one grain interacts with its neighboring grains will affect the magnitude of stress or stress concentration. Therefore, a better understanding of grain interactions and GB behavior is the key to improve the fatigue property including crack initiation and propagation.

However up to now, there is still a lack in experimental and numerical evidences for the capability of different orientations in relieving stress formation and concentration in aluminum alloys. There are some reports for hexagonal close-packed (HCP) metals about how grains interact with each other [6,7]. Luster et al. [6] first defined a geometric compatibility factor to describe GB deformation in Ti-Al alloys. This factor only considered the contribution from active slip planes normal and slip directions for two neighboring grains. Recently, Sun et al. [7] proposed a new factor to measure strain accommodation around GB interface in magnesium alloys by experimental methods. Comparatively, this new factor not only considers the contribution from geometric compatibility factor, but also Schmid factor (SF). However, the primary deformation modes in HCP metals are the basal slip and {10–12} tension twin [8]. As we know, there are only 3 slip systems in HCP metals, but there are 12 slip systems in face-centered cubic (FCC) aluminum alloys. As well known, the number of slip system plays an important role in affecting grain deformation behavior and corresponding grain interaction. Therefore, the mechanism about grain interactions in HCP metals cannot fully provide guidance for interaction mechanism in FCC aluminum alloys. There are some literatures about grain or GB deformation behavior in aluminum alloys [9–11]. In 2002, Sachtleber et al. [9] found by an experimental approach that grain-scale strain was heterogeneous in aluminum during plastic deformation. They reported that the strain pattern during plane strain compression was strongly determined by the orientation dependence of the kinematic hardness of the individual grains. Similarly, by an experimental investigation in Al-0.5%Mg multicrystal, Zhang et al. [10] found that this alloy obeyed neither the Sachs nor the Taylor polycrystal deformation models, but deformed in a heterogeneous way to favor easy slip transmission and accommodation among the grains. Besides, by the in-situ Electron Back-Scattered Diffraction (EBSD) investigation in aluminum alloy, Chen et al. [11] revealed that the grains rotated gradually with increasing strain during tensile deformation, and the rotation behavior could be adequately described by the activation of two slip systems corresponding to the maximum and second maximum SFs. From the above review, it is clear that the deformation behavior within grains or at GBs in aluminum alloys is far different from HCP metals. Multi-slipping is the main feature in aluminum alloys and the corresponding grain or GB deformation mechanisms are influenced by SF, the number of slip system, and grain orientations.

There are two main numerical methods for investigating plasticity deformation behavior of crystal, namely Molecular Dynamics (MD) and Crystal Plasticity Finite Element Method (CPFEM). To our best knowledge, MD is suitable for analyzing the physical movements of atoms and molecules, and plays an important role in revealing the micro-mechanism of plasticity deformation behavior of crystals [12,13]. However, the calculation size of MD is very small, usually in the level of nanometer. As a result, MD is difficult to provide relatively accurate prediction for the macroscale experimental results of mechanical properties, such as strength and fatigue of materials. Comparatively, CPFEM is an extremely versatile tool for describing the mechanical response of crystalline materials on all length scales from single crystals to engineering parts. The research value of the present work is to provide guidelines for how to improve macroscale fatigue property of AA2024 from the aspect of stress formation. Therefore, CPFEM is adopted to investigate stress formation behavior in present work. Up to now, CPFEM technique has been used extensively in order to predict the evolution of grain orientation during deformation [14–16] as well as the in-grain heterogeneity of plastic strain [17–19] and the resulting lattice orientation spreads [20–22]. In CPFEM, one important topic is about grain or GB interaction. Some grain or GB interaction modellings based on dislocation interactions have been built up [23–26]. In those CPFEM models, it is generally accepted that GB is regarded as a perfectly sharp interface. In other words, GB possesses zero thickness and no relative displacement is allowed across GB. As a result, the physical properties including elastic modulus tensor and slip direction alter abruptly across GB. To this day, CPFEM has only seldom been used to predict the dependence of stress formation associated to a given texture or GB, and the related research is unavailable. Recently, Cheng et al. [27] have demonstrated by a two-dimensional CPFEM on polycrystalline copper that texture orientation has a stronger dependence on GB sliding than stress exponent, and the stress concentration at GBs caused by GB sliding also induces a redistribution of stress in the grain interior. This also reveals that the bridge factors between GB stress formation and grain orientation are essentially correlated to dislocation slipping. But still, there lacks a systematical investigation about the relationship between stress formation at GBs and dislocation slipping-related impact factors. To the best of our knowledge, the stress formation within grain or at GB is a key for controlling fatigue crack initiation and propagation. In 2xxx series aluminum alloys, main textures include Goss, Cube, Brass, Copper, S and random components, and by combining any two of them there is a lot of GB types [28,29]. A systematical understanding of grain interactions at different orientation combination by using CPFEM will be very useful for understanding the fatigue mechanisms dominated by the effect of grain orientation.

In view of limited numerical studies on the dependence of stress formation associated to a given texture or GB, this study presents a dislocation-based constitutive monocrystal and bicrystal model to investigate grain orientation effect on stress formation within monocrystal and at GB. This paper is organized as follows. In Section 2, the constitutive frameworks of monocrystal and bicrystal model used in this study are outlined for a typical Al-Cu-Mg alloy (AA2024). In Section 3.1, stress formation with monocrystal is investigated based on the Schmid factor (SF) difference. In Section 3.2, stress formation at GB is comparatively investigated by correlating its original stress at corresponding monocrystals. Finally, In Section 3.3, the dependence relations are discussed between GB stress and corresponding correlation factors, such as geometric compatibility factor, comprehensive factor, and an advanced comprehensive factor combining SF, and geometry compatibility factor for 5 independent slip systems. Specially, considering the important role played by Goss and Cube grains in improving fatigue resistance of AA2024, the main focus

from Sections 3.1 to 3.3 is directed towards the dependence of stress formation on Goss and Cube monocrystals, and Goss-participated and Cube-participated GBs.

2. Numerical procedures

2.1. Finite element models

Firstly, a monocrystal model as shown in Fig. 1 is used for the stress simulations under the action of tensile loading. According to our previous research [30], Goss and Cube are the preferred orientations, and their size can reach 1 mm at most. But the sizes of Goss and Cube are mainly located at the range of 100 to 300 μm. Therefore, the monocrystal size is set to 250 × 200 × 5 μm. When the load direction is parallel to rolling direction, the length is 250 μm in rolling direction (RD), the width is 200 μm in transverse direction (TD), and the thickness is 5 μm in normal direction (ND) vertical to RD-TD plane (Fig. 1). In this case, the boundary of crystal at one side is fixed, where the displacement in *x*, *y* and *z* are set into 0. At another side, an increase of 3% displacement parallel to RD is employed, and at the same time the displacements in *y* and *z* directions are fixed. This fixation in the *y* and *z* directions will effectively compel the other slip systems with low SF to be activated during 3% strain (ε). It is worthy to note that this 3% deformation can guarantee the activation of all 12 slip systems for all grain orientations. All meshes make use of C3D8 element type and are in the shape of 5 × 5 × 5 μm cube. In order to fully investigate the effect of load direction, the loading at traverse direction (TD) is also employed. When the load direction is parallel to TD, then the model length in TD is 250 μm, and other parameters are all the same as in RD. The strain rate ($\dot{\varepsilon}$) for monocrystal simulations is 3 × 10^{-2} s^{-1}, and simulation temperature is a constant at 25 °C. Beside for any given orientations, the comprehensive pole figures collected from all nodes of model are obtained before and after deformation using texture analysis software Mtex. The relative details about Mtex software can be found in Refs. [31,32].

Furthermore, a bicrystal model as shown in Fig. 2a is also used to simulate the stress formation at grain boundary (GB). In this model, the different color represents different oriented crystal. The size of bicrystal model consisted by grains *a* and *b* is set to 350 × 200 × 5 μm, and the GB is making an angle of 60° with loading direction. When the load direction is parallel to rolling direction, the length in RD is 350 μm, as shown in Fig. 2a. In this case, the boundary of bicrystal at one side is fixed, where the displacements in *x*, *y* and *z* are set into 0. At another side, a 3% displacement parallel to RD is employed, and simultaneously the displacements in *y* and *z* direction are fixed. Also, similar with monocrystal model,

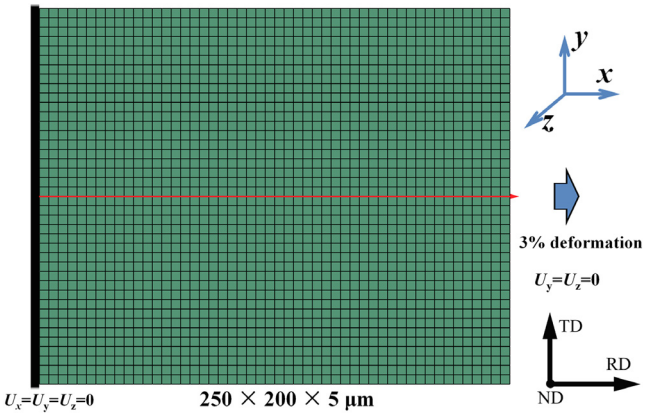

Fig. 1. The model for monocrystal.

the C3D8-element mesh is employed for this bicrystal model (the corresponding grain interaction conditions at boundary are presented in Section 2.2). The strain rate for all bicrystal simulations is 3 × 10^{-2} s^{-1}, and simulation temperature is a constant at 25 °C. By considering the strong dislocation interaction at GB, the mesh size gradually decreases by decreasing the distance to GB in order to obtain accurate simulation results. A high magnification at GB is shown in Fig. 2b, and after deformation the corresponding stress formation at different node along the red line can be collected. Considering in the field of Extended Finite Element Method (XFEM), the Maximum Principal Stress (MAXPS) criterion is widely used for predicting crack initiation or propagation in Al alloys. It is assumed that crack initiation or propagation will begin when the largest principal stress reaches a specified certain value [33,34]. Although, the use of MAXPS criterion results in certain errors with real experimental results, it anyway indicates that the magnitude of stress is a key parameter affecting fatigue crack initiation or propagation. Therefore, we will focus in the present work to evaluate stress dependence on grain orientation and GB type. From our previous research [30], it was found that Goss grain mainly grew into Brass grain. Cube grain could mainly grow into S and also into Brass and Copper at specific temperature range. However, some portion of Brass, Copper and S could always retain after recrystallization. Therefore, the main considered boundaries in the present bicrystal model are Goss-Brass, Cube-S, Cube-Brass and Cube-Copper types. Also, it should be noted that although Goss grain cannot grow into Copper and S grains, Goss-Copper and Goss-S boundaries are also present when Goss grain consumes Brass grain and then comes across Copper and S grains. In addition, random grains could also grow into Brass, Copper and S grains during recrystallization, and correspondingly the boundaries between random grains and deformed grains (Brass, Copper and S) are also considered. In the present work, 10 random grains are chosen, and their crystal space orientations can be found in Fig. 2c. The {1 1 0} and {1 1 1} pole figures for these 10 random grains are shown in Fig. 2d. It can be seen that the orientation distribution is relatively homogeneous in the stereographic projection, which indicates that the present 10 random grains contain relatively possible all other positions except specific orientations in Euler space.

2.2. Crystal plasticity model

In present simulation, the constitutive laws for monocrystal and bicrystal are elaborated in details as follows. For monocrystal, based on the theory of crystal plasticity, the deformation gradient tensor *F* can be expressed by [35,36]:

$$F = \frac{\partial x}{\partial X} = F_e \cdot F_p \tag{1}$$

where, *X* and *x* represent the crystal position of space configuration before and after deformation, respectively. As shown in Fig. 3, the deformation gradient tensor *F* can be decomposed into elastic and plastic components, F_e and F_p, respectively. The elastic part F_e comprises the small lattice deformation and possibly large rigid body rotation. The plastic part F_p corresponds to the isoclinic and stress-free intermediate configuration, in which the crystallographic lattice is unaltered and unrotated with respect to the reference configuration. Specifically, we use *L* to represent the total velocity gradient and it can be defined as:

$$\begin{aligned} L &= \frac{\partial v}{\partial x} = \frac{\partial v}{\partial X} \cdot \frac{\partial X}{\partial x} = \dot{F} \cdot F^{-1} = \dot{F_e} \cdot F_e^{-1} + F_e \cdot (\dot{F_p} \cdot F_p^{-1}) \cdot F_e^{-1} \\ &= L_e + F_e \cdot L_p \cdot F_e^{-1} \end{aligned} \tag{2}$$

where, L_e is elastic velocity gradient and L_p is plastic velocity gradient. Besides, based on the generalized Hooke's law [37], the rela-

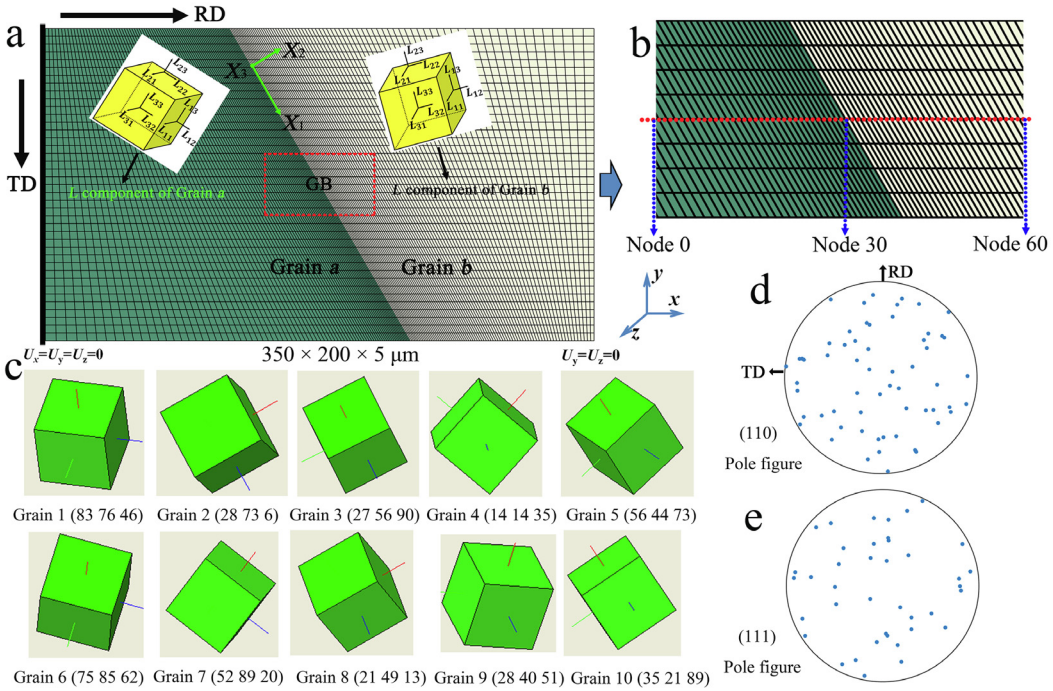

Fig. 2. The bicrystal model for AA2024 alloy: (a) the model details, (b) a high magnification at grain boundary, (c) 10 random oriented grains and (d) the pole figure for those 10 random grains.

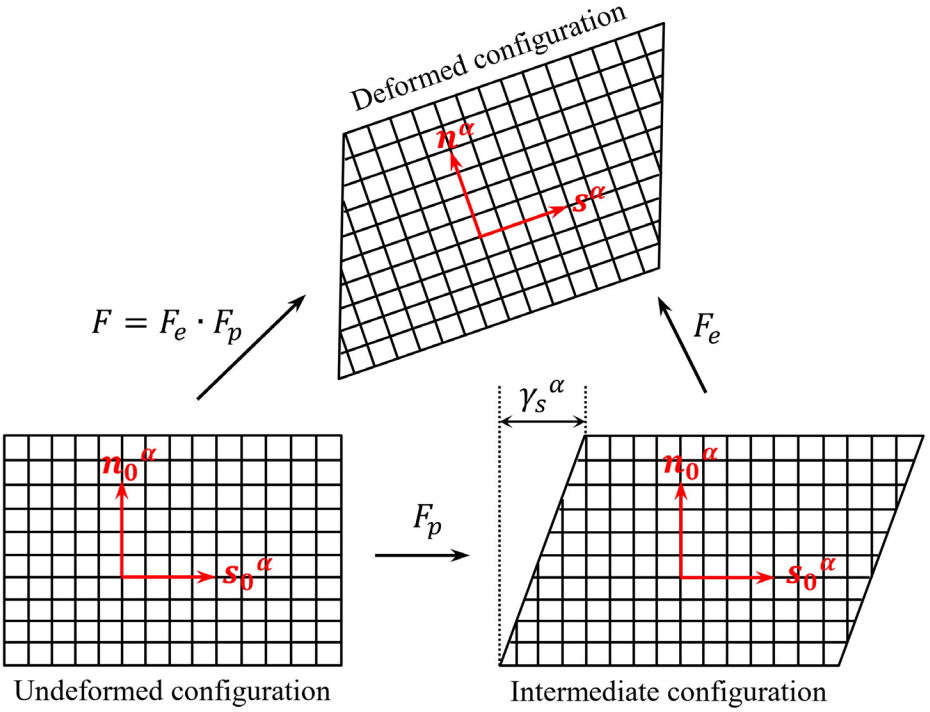

Fig. 3. Multiplicative decomposition of the deformation gradient tensor.

tionship between the second Piola-Kirchhoff stress tensor S and the Green-Lagrange strain tensor E can be expressed as:

$$S = C : E \tag{3}$$

where C is the fourth-order elastic tensor, and strain tensor E can be further defined by:

$$E = \frac{1}{2}(F_e{}^T F_e - I) \tag{4}$$

In which, $F_e{}^T$ is the transpose of F_e, and I is the identity tensor. Relating the elastic deformation gradient tensor (F_e) with slip system, the evolution of the elastic deformation part can be expressed as:

$$s^{\alpha} = F_e \cdot s_0{}^{\alpha} \tag{5}$$

$$n^{\alpha} = n_0{}^{\alpha} \cdot F_e{}^{-1} \tag{6}$$

where,$s_0{}^{\alpha}$is the original unit vector along α^{th} slip direction, and $n_0{}^{\alpha}$ is the original unit vector along the normal direction of α^{th} slip plane. For the part of plasticity, $L_p$can be written as:

$$L_p = \dot{F_p} \cdot F_p{}^{-1} = \sum_{\alpha=1}^{N_s} \dot{\gamma}_s{}^{\alpha} (s_0{}^{\alpha} \otimes n_0{}^{\alpha}) \tag{7}$$

where $\dot{\gamma}_s{}^{\alpha}$ is the shear strain rate on α^{th} slip direction, and N_s is the total number of slip systems. The material investigated is a standard AA2024-T3 alloy. According to Refs. [3,38], only {111} ⟨110⟩ slip system can be activated at room temperature deformation for 2xxx series Al alloys. Therefore, only {111} ⟨110⟩ slip system is considered in the present simulation and the value of $N_s$is 12. Besides, the symbol ⊗ represents tensor product. For example, givings$_0{}^{\alpha}$ = [$u_0{}^{\alpha} v_0{}^{\alpha} w_0{}^{\alpha}$] and$n_0{}^{\alpha}$ = [$h_0{}^{\alpha} k_0{}^{\alpha} l_0{}^{\alpha}$], then the $s_0{}^{\alpha} \otimes n_0{}^{\alpha}$ can be calculated as:

$$s_0{}^{\alpha} \otimes n_0{}^{\alpha} = \begin{bmatrix} u_0{}^{\alpha} h_0{}^{\alpha} & u_0{}^{\alpha} k_0{}^{\alpha} & u_0{}^{\alpha} l_0{}^{\alpha} \\ v_0{}^{\alpha} h_0{}^{\alpha} & v_0{}^{\alpha} k_0{}^{\alpha} & v_0{}^{\alpha} l_0{}^{\alpha} \\ w_0{}^{\alpha} h_0{}^{\alpha} & w_0{}^{\alpha} k_0{}^{\alpha} & w_0{}^{\alpha} l_0{}^{\alpha} \end{bmatrix} \tag{8}$$

Based on dislocation theory, the shear strain rate $\dot{\gamma}_s{}^{\alpha}$ or shear rate on the α^{th} slip system can be modeled using a classic rate-dependent phenomenological Norton-type law [39]:

$$\dot{\gamma}_s{}^{\alpha} = \begin{cases} \dot{\gamma_0} \left| \frac{\tau^{\alpha} - \chi^{\alpha}}{\tau_c{}^{\alpha}} \right|^n sgn(\tau^{\alpha} - \chi^{\alpha}), if |\tau^{\alpha}| \geq \tau_c{}^{\alpha} \\ 0, if |\tau^{\alpha}| < \tau_c{}^{\alpha} \end{cases} \tag{9}$$

where, $\dot{\gamma_0}$ is the reference shear rate, and τ^{α} is the resolved shear stress that can be written as:

$$\tau^{\alpha} = \sigma : (s^{\alpha} \otimes n^{\alpha}) \tag{10}$$

where, $\sigma$is Cauchy stress tensor. Essentially, slip systems are related to dislocation movement. Therefore, the resolved shear stress (τ^{α}) can also be further written as a function of dislocation densities of each system [40,41]:

$$\tau^{\alpha} = 0.3 \mu b \sqrt{\sum_{\beta} a^{\alpha\beta} \rho^{\beta}} \tag{11}$$

where μ is the shear modulus, and b is the magnitude of Burger vector. $a^{\alpha\beta}$ is a component of the dislocation interaction matrix coefficient, which gives the interaction between slip systems (α) and (β). If α equals to β, $a^{\alpha\beta}$ is set to 0.2 in the present work; if α does not equal to β, it is set to 0.35 [42]. ρ represents the total dislocation densities caused by one specific slip system, and will evolve with the course of deformation. The evolution of these dislocation densities caused by α^{th} slip system during deformation can be further calculated as [43]:

$$\dot{\rho}^{\alpha} = \frac{|\dot{\gamma}_s{}^{\alpha}|}{b} \left(\frac{\sqrt{\sum_{\beta} a^{\alpha\beta} \rho^{\beta}}}{K} - 2 y_c \rho^{\alpha} \right) \tag{12}$$

where K is the material parameter, and y_c is a physical parameter that describes the annihilation distance of dislocations. If two dislocations of same slip system (α) cross themselves at a distance smaller than y_c, then they can annihilate together. In Eq. (9), $\tau_c{}^{\alpha}$ is Critical Resolved Shear Stress (CRSS) or slip resistance that can be expressed using a Voce law [44]:

$$\tau_c{}^{\alpha} = \tau_0{}^{\alpha} + \tau_1{}^{\alpha} \left(1 - \exp\left(-\frac{b_1{}^{\alpha}}{\tau_1{}^{\alpha}} \Gamma_s \right) \right) \tag{13}$$

where $\tau_0{}^{\alpha}$, $\tau_0{}^{\alpha} + \tau_1{}^{\alpha}$, $b_1{}^{\alpha}$ are the initial slip resistance, the saturated slip resistance and initial hardening rate, respectively. $\Gamma_s$is total accumulated shear strain.

Besides, the time derivative of $\tau_c{}^{\alpha}$represents the hardening of CRSS, and correspondingly it can be calculated as:

$$\dot{\tau_c}{}^{\alpha} = \frac{d\tau_c{}^{\alpha}}{dt} = b_1{}^{\alpha} \exp\left(-\frac{b_1{}^{\alpha}}{\tau_1{}^{\alpha}} \Gamma_s \right) \cdot \frac{d\Gamma_s}{dt} \tag{14}$$

From Eq. (13), it is understood:

$$\frac{d\tau_c{}^{\alpha}}{d\Gamma_s} = b_1{}^{\alpha} \exp\left(-\frac{b_1{}^{\alpha}}{\tau_1{}^{\alpha}} \Gamma_s \right) \tag{15}$$

Besides, the time derivative of Γ_s is actually the sum of shear strain rate contributed by all slip systems, and it can be expressed as:

$$\frac{d\Gamma_s}{dt} = \sum_{\beta=1}^{N_s} q^{\alpha\beta} \left| \dot{\gamma}_s{}^{\beta} \right| \tag{16}$$

where $q^{\alpha\beta}$ is the hardening matrix coefficient considering the effect of the slip system β over the slip system α. When α equals to β, $q^{\alpha\beta}$ is set to 1, and when α does not equal to β, it is set to 1.4 [45]. So, the time derivative of $\tau_c{}^{\alpha}$can be further written as:

$$\dot{\tau_c}{}^{\alpha} = \frac{d\tau_c{}^{\alpha}}{d\Gamma_s} \sum_{\beta=1}^{N_s} q^{\alpha\beta} \left| \dot{\gamma_s}{}^{\beta} \right| \tag{17}$$

Based on the Schmid criterion, we should also understand that the α^{th} slip system will be activated as long as τ^{α} is equal to or more than $\tau_c{}^{\alpha}$. This will finally contribute to the formation of dislocation or dislocation densities. Besides, in Eq. (9), χ^{α} is the back-stress on the α^{th} slip system. The kinematic evolution of back-stress follows a pure nonlinear kinematic hardening rule of the Armstrong-Frederick law [46]:

$$\dot{\chi}^{\alpha} = h \dot{\gamma}_s{}^{\alpha} - h_d |\dot{\gamma}_s{}^{\alpha}| \chi^{\alpha} \tag{18}$$

where h and h_d are the direct hardening and dynamic recovery coefficients, respectively. The investigated material is a typical 2xxx series aluminum alloy (AA2024-T3), and the all estimated crystal plasticity parameters given in Table 1 are obtained from Refs. [42,47–50].

From the above constitutive law, the internal stress within monocrystal is directly dependent on dislocation densities caused by dislocation-slipping accumulation. Considering the different resolved shear stress (τ^{α}) at different slip systems and the existence of multi-slipping, the deformation within monocrystal is therefore heterogeneous and also a result of the activation of all possible slip systems. This conforms the fourth strength theory of

Table 1
Employed CP parameters for AA2024 alloy [42,47–50].

Property	Unit	Value
C_{11}	[GPa]	112
C_{12}	[GPa]	59.5
C_{44}	[GPa]	26.7
$\dot{\gamma_0}$	[s^{-1}]	1e-3
n	[–]	10
$\tau_0{}^{\alpha}$	[MPa]	76
$\tau_1{}^{\alpha}$	[MPa]	82.5
$b_1{}^{\alpha}$	[MPa]	1810
μ	[GPa]	26.5
b	[nm]	0.285
K	[–]	38
y_c	[nm]	0.957
h	[MPa]	3600
h_d	[–]	380

materials mechanics (maximum distortion-energy theory), and correspondingly von Mises stress (σ_m) is used in present simulation to represent the stress value at any point of monocrystal. In the present monocrystal modelling, the constitutive equation between von Mises stress (σ_m) and total dislocation density (ρ_{total}) is used as [37,51]:

$$\sigma_m = 20 + 0.3\mu b\sqrt{\rho_{total}} = 20 + 0.3\mu b\sqrt{\sum_{\beta} a^{\alpha\beta}\rho^{\beta}}(\mathrm{MPa}) \tag{19}$$

Therefore, it is also clear that von Mises stress (σ_m) is positively correlated with total dislocation density.

For the bicrystal model, beside the constitutive law of monocrystal, the interaction between two conterminous crystals needs to be considered along GB. In other words, the corresponding constitutive law at GB needs to be increased for bicrystal model. Based on the method proposed by Kanjarla and Houtte et al. [24,25], one ideal GB model is developed in the present simulation to consider the coordinate deformation for GB and bicrystals. Compared with Ref. [24,25], the present GB model adds the role of dislocation, and is a dislocation-based constitutive GB model. The algorithm about GB compatible deformation is described as follows. First, due to the inhomogeneous distribution for deformation velocity and stress within each crystal, it is necessary to describe the velocity and stress not over a given area but at a specific point in the crystals. The velocity gradient tensor (L) and Cauchy stress tensor (σ) at any point can be defined by nine components. The velocity gradient tensor (L) with nine components at GB coordinate system is shown in Fig. 2a, and the coordinate direction of Cauchy stress tensor (σ) component is same with L. In GB coordinate system, the direction along X_1 is parallel with GB interface. The direction along X_2 is perpendicular to GB interface, and the direction along X_3 is vertical to paper plane. Specifically in the form of tensor, L and σ can be expressed, respectively, as:

$$L = \begin{bmatrix} L_{11} & L_{12} & L_{13} \\ L_{21} & L_{22} & L_{23} \\ L_{31} & L_{32} & L_{33} \end{bmatrix}, \mathrm{and}\sigma = \begin{bmatrix} \sigma_{11} & \sigma_{12} & \sigma_{13} \\ \sigma_{21} & \sigma_{22} & \sigma_{23} \\ \sigma_{31} & \sigma_{32} & \sigma_{33} \end{bmatrix} \tag{20}$$

We assume that grains are separated by planar GBs that are perfect, without damage and GB sliding. Also, no relative displacement is allowed across the GB. The corresponding GB geometry characteristic can be described by five macroscopic degrees of freedom [52]. Three degrees of freedom define the relative misorientation between crystal lattices of two neighbouring grains, described as $(UVW)/\theta$ relationship where (UVW) is the rotation axis and θ is the rotation angle. The other two degrees of freedom define the GB planes, i.e., $(H_aK_aL_a)$ for grain a and $(H_bK_bL_b)$ for grain b. In the present GB model, it is clear that these five degrees of freedom ($(UVW)/\theta$, $(H_aK_aL_a)$ and $(H_bK_bL_b)$) are only determined by the miller index or Euler angle of two grain a and b. Then, for guaranteeing GB compatible deformation and at the same time the two grains cooperatively accommodate the deformation, the local velocity gradient tensor (L^g) and the local stress tensor (σ^g) at GB constructed by grain a and b need to satisfy the direct balance conditions:

$$L_{ij}{}^{g}{}_{agrain} = L_{ij}{}^{g}{}_{bgrain}, i = 1,2,3 and j = 1,3 \tag{21}$$

$$\sigma_{i2}{}^{g}{}_{agrain} = \sigma_{i2}{}^{g}{}_{bgrain}, i = 1,2,3 \tag{22}$$

In other words, the corresponding velocity gradient tensor components need to be equal on the GB interface for grain a and b (in the present case, they are 11, 13, 21, 23, 31 and 33 as presented in Eq. (21)). Also, the corresponding stress components need to be equal on the interface the two grains (these are 12, 22, and 32 as presented in Eq. (22)). Besides, GB deformation needs to be indirectly restricted by considering compatible grain interaction in bicrystal model because GB is the place where grain interaction takes place. For realizing the compatible grain interaction in bicrystal model, the shear strain rate ($\dot{\gamma}_s{}^{\alpha}$) in Eq. (9) for grain a and b needs to satisfy the velocity compatibility condition [25]:

$$\dot{\gamma}_s{}^{\alpha} = \frac{L_{ij} + L_{ji}}{2M_{\alpha ij}} \tag{23}$$

In which $M_{\alpha ij}$ are constants that for grain a and b are equal to $(n_ib_j + n_jb_i)/2$. n is the unit vector normal to the slip plane, and b is the unit vector parallel with the slip direction. So, in this case, combining with Eq. (12), the evolution of dislocation densities ($\dot{\rho}^{\alpha}$) caused by α^{th} slip system for the two grains can be further expressed as:

$$\dot{\rho}^{\alpha} = \frac{|L_{ij} + L_{ji}|}{2bM_{\alpha ij}}\left(\frac{\sqrt{\sum_{\beta} a^{\alpha\beta}\rho^{\beta}}}{K} - 2y_c\rho^{\alpha}\right) \tag{24}$$

It is clear that solving the Eqs. (23) and (24) will lead to the restriction on GB shear strain rate by confining dislocation density evolution in bicrystal model. Finally, in order to satisfy the Schmid law for bicrystal model, the rate of plastic work (P^*) taken in the two grains a and b, should be minimized, i.e.:

$$P^* = \sum_{\alpha=1}^{N_s} \tau_c{}^{\alpha}\left|\dot{\gamma}_s{}^{\alpha}\right| = min \tag{25}$$

This also means that the shear strain rate ($\dot{\gamma}_s{}^{\alpha}$) and critical resolved shear stress ($\tau_c{}^{\alpha}$) for these two grains should all be satisfied for extreme conditions. Combining with Eq. (12), Eq. (25) can be further expressed as follows:

$$\sum_{\alpha=1}^{N_s} \frac{K\tau_c{}^{\alpha}\dot{\rho}^{\alpha}b}{\left(\sqrt{\sum_{\beta} a^{\alpha\beta}\rho^{\beta}} - 2Ky_c\rho^{\alpha}\right)} = min \tag{26}$$

As we know, both parameters $\tau_c{}^{\alpha}$ and ρ are functions of time or strain. In order to satisfy the Schmid law, $\tau_c{}^{\alpha}$ and ρ should be restrained into certain values where the rate of plastic work is a minimum value. As a result, solving the Eqs. (25) and (26) will also lead to the corresponding restriction on GB plastic work rate by confining ρ and$\tau_c{}^{\alpha}$ in bicrystal model. It is worthy to note that the von Mises stress (σ_m) at GB is still a function of total dislocation density (ρ_{total}). However, total dislocation density (ρ_{total}) at GB cannot be calculated according to Eq. (19). In this case, GB stress is not only decided by the total dislocation density at each monocrystal, but also dislocation-slip interaction behavior at GB. Actually in present bicrystal modelling, the corresponding constitutive law between von Mises stress (σ_m) and dislocation interaction is very complex to define. However, by solving Eqs. (21)–(26), the qualitative relationship between GB stress and dislocation-slip interaction can be obtained. In the present work, the research purpose for bicrystal modelling is to analyze the dependence of GB stress on grain interaction related to Schimid factor and slip system interactions.

The modelling details can be summarized by the flowchart presented in Fig. 4. The material model is first implemented in ABAQUS Explicit via the user subroutine UMAT connected to the CPFEM FORTRAN code. The subroutine gathers the deformation gradient tensors followed by the initialization of slip systems for each integration point. Then, the resolved shear stresses (τ^{α}), shear strain rates ($\dot{\gamma}_s{}^{\alpha}$), the evolution of dislocation densities ($\dot{\rho}^{\alpha}$) and deformation gradient components are calculated for each slip system. For bicrystal model, the local stresses (σ^g) tensor and velocity gradient tensor (L^g) balance equations need to be solved. And also, the shear strain rate ($\dot{\gamma}_s{}^{\alpha}$) or the evolution of dislocation densities

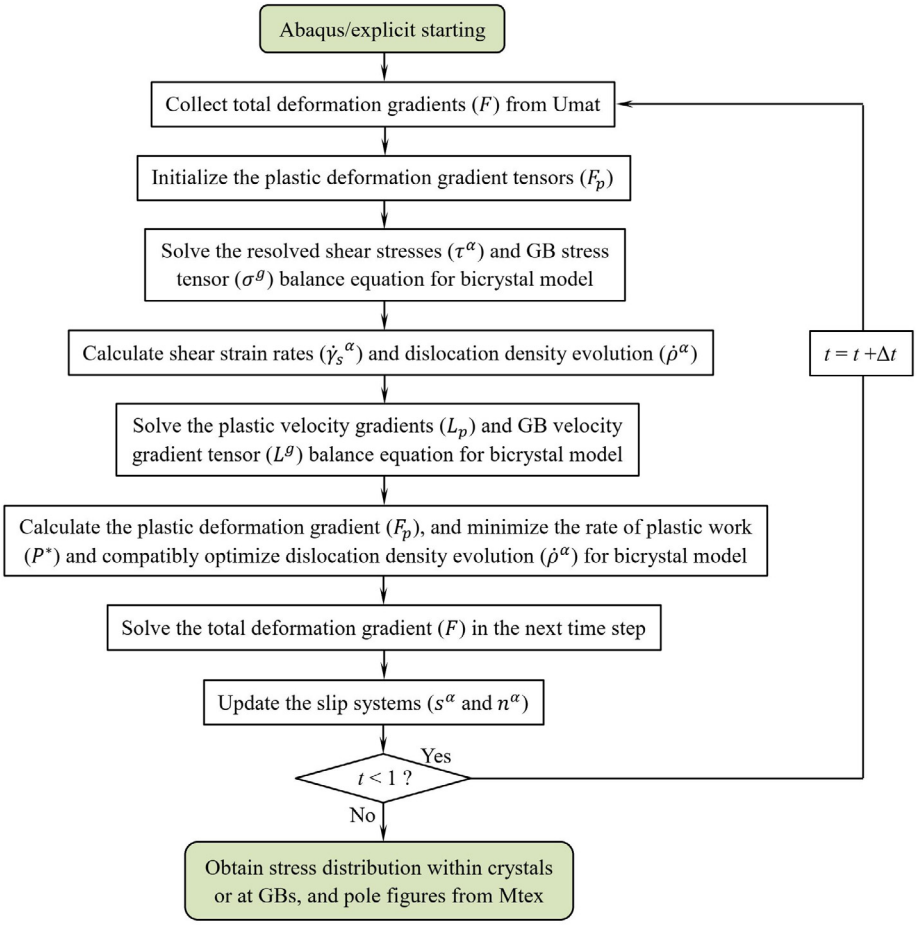

Fig. 4. The flowchart of CPFE model.

($\dot{\rho}^{\alpha}$) is necessary to satisfy the corresponding compatibility conditions. In addition, the rate of plastic work (P^{*}) is minimized, which will also lead to the compatible optimization for the evolution of dislocation densities ($\dot{\rho}^{\alpha}$). It is worthy to note that during the calculation process, once any resolved shear stress (τ^{α}) in the slip system reaches its critical resolved shear stress ($\tau_c{}^{\alpha}$), the slip is activated and the crystal begins to plastically deform by dislocation slip on this system. As the displacement is increased, the resolved shear stress may be reached on the $\tau_c{}^{\alpha}$ of other slip systems and then these systems begin to be activated. As a result, multiple slips probably occur simultaneously during the employing displacement process. The subroutine will recalculate the plastic shear strain rates, dislocation densities evolution, deformation gradients, and slip systems after the calculation loop finishes for each time increment. Finally, when the total time reaches 1, the modelling of CPFEM ends, and the stress data about crystals or at GBs and pole figures by using Mtex software can be correspondingly obtained.

2.3. Calculation of Schmid factor (SF)

Considering the predominated role of SF in controlling the magnitude of stress formation, the SFs are thereby calculated for monocrystal and bicrystals models. In the simulation, the definition of grain orientation is given by Euler angle ($\varphi_1, \psi, \varphi_2$). Then the Miller index (h)[u] of this grain can be obtained by rotation matrix g that is written as [53]:

$$g = \begin{pmatrix} cos\varphi_1 cos\varphi_2 - cos\psi sin\varphi_1 sin\varphi_2 & -cos\psi cos\varphi_2 sin\varphi_1 - cos\varphi_1 sin\varphi_2 & sin\varphi_1 sin\psi \\ cos\varphi_2 sin\varphi_1 + cos\varphi_1 cos\psi sin\varphi_2 & cos\varphi_1 cos\psi cos\varphi_2 - sin\varphi_1 sin\varphi_2 & -cos\varphi_1 sin\psi \\ sin\psi sin\varphi_2 & cos\varphi_2 sin\psi & cos\psi \end{pmatrix} \tag{27}$$

Correspondingly for this g matrix, h and u can be, respectively, expressed as:

$$h = (sin\varphi_1 sin\psi - cos\varphi_1 sin\psi cos\psi) \tag{28}$$

$$u = (cos\varphi_1 cos\varphi_2 - cos\psi sin\varphi_1 sin\varphi_2 cos\varphi_2 sin\varphi_1 + cos\varphi_1 cos\psi sin\varphi_2 sin\psi sin\varphi_2) \tag{29}$$

After having the information of grain Miller index (h)[u], then the SF (k^{α}) for α^{th} slip system of this grain can be expressed as [54]:

$$k^{\alpha} = cos\phi^{\alpha} \cdot cos\lambda^{\alpha} = \frac{(s^{\alpha} \cdot f) \cdot (n^{\alpha} \cdot f)}{|s^{\alpha}||n^{\alpha}|\left|f^{2}\right|} \tag{30}$$

where ϕ^{α} is the angle between force direction (f) and the normal direction of α^{th} slip plane (n^{α}), and λ^{α} is the angle between force direction (f) and α^{th} slip direction (s^{α}). The value of α is equal to 1, 2, 3,..., 12. When the load direction is parallel with RD, f can be expressed as f = u. When the load direction is parallel with TD, it can be expressed as f=h × u. For bicrystals model, the SF for the α^{th} slip system of grain a and b can be written, respectively, as:

$$k_a{}^{\alpha} = \frac{(s_a{}^{\alpha} \cdot f_a) \cdot (n_a{}^{\alpha} \cdot f_a)}{|s_a{}^{\alpha}| \cdot |n_a{}^{\alpha}| \cdot \left|f_a{}^{2}\right|} \tag{31}$$

$$k_b^{\alpha} = \frac{(s_b^{\alpha} \cdot f_b) \cdot (n_b^{\alpha} \cdot f_b)}{|s_b^{\alpha}| \cdot |n_b^{\alpha}| \cdot |f_b^2|} \quad (32)$$

where n_a^{α} is the α^{th} slip plane normal direction of grain a and s_a^{α} is the α^{th} slip direction of grain a. n_b^{α} is the α^{th} slip plane normal direction of grain b and s_b^{α} is the α^{th} slip direction of grain b. f_a and f_b are the force direction of grain a and b, respectively. When the load direction is parallel with RD, it can be calculated as $f_a = u_a$ and $f_b = u_b$, respectively. When load direction is parallel with TD, it can be calculated as $f_a = h_a \times u_a$, and $f_b = h_b \times u_b$, respectively.

3. Results and discussions

3.1. Stress formation at monocrystal

In the present work, the formed stress within monocrystal is obtained according to Eq. (19). Therefore, the relationship between stress formation and dislocation density does not need to be discussed. As we understand, grain orientation effect on stress formation is essentially contributed to the difference in Schmid factor (SF) connected with slip systems. Therefore, we focus on the relationship between stress formations within different orientations and slip systems with different SFs. The simulated von Mises stress of monocrystal along ND is found to be almost unchanged, so only the stress distribution at RD-TD plane after deformation for different grain orientations is shown in Fig. 5. It can be seen that the stress distribution at Goss and Cube grains is symmetrical along RD and TD. It means that the corresponding dislocation density distribution has also same symmetry along RD and TD. Comparatively, the stress distribution at Copper only shows a good symmetry along RD. For Brass and S grains, no stress symmetry along RD or TD can be observed. This symmetry of grain orientation is also revealed from crystal shape or orientation. As it can be seen, the geometry shape of Goss and Cube is symmetrical at both RD and TD direction, and Copper also shows stress symmetry only along RD. Brass and S crystals fail to show any symmetry along RD or TD. This strong symmetry leads to the formation of more equivalent slip systems. As presented in Table 2 later, the equivalent slip systems with the maximum SF for Cube and Goss are all 8. In present work, the slip systems with equal maximum SF values are called as equivalent initial slip system (EISS). The EISS for Copper, Brass and S is 6, 2 and 1 respectively. It is clear that the stronger crystal geometrical symmetry or higher EISS number will be beneficial for the more symmetrical stress distribution. Fig. 6 shows a quantitative stress comparison for different orientations, where the stress values are obtained along the red line in Fig. 1. There is a large fluctuation of stress at the two sides of crystals after the 3% displacement deformation, which is attributed to the effect of boundary conditions. For the stress corresponding to the distance from 1 to 24 μm, there is almost no difference for Cube and Goss crystals. Compared with Brass, Copper and S orientation, Goss and Cube show a better ability in relieving stress concentration. Of Brass, Copper and S orientations, Copper shows the highest value of stress (340.8 MPa in average) and Brass shows the lowest one (251.0 MPa in average). The average stress value for S is in between Brass and Copper. In addition, it is well known that the stress formation is a dynamic process during deformation and is strongly associated with dislocation dynamics [55]. In the light of this, the relationship between average stress and nominal strain (ε) for these 5 orientations during deformation is shown in Fig. 7. It is clear that stress evolution for all 5 orientations is similar and consists of two stages, corresponding to elastic and plastic deformations, respectively. For the elastic stage, the average stress of crystals will gradually increase with increasing strain. When the strain reaches a certain value that corresponds to monocrystal yield point, crystals start to enter into the stage of plastic deformations, and the slope in stress increase with strain obviously decreases compared with elastic stage. By comparing these 5 orientations, the average stress of S crystal at any strain is always the highest one. Although there is no obvious stress difference for Brass and S crystals when the strain is smaller than 0.0034, after that, S crystal always has higher stress formation than Brass at same strain. Also as expected, the stress evolution of Goss and Cube crystals is almost the same during deformation, and their average stresses are always lower than Brass, Copper and S. From the present results, it is clear that Goss and Cube have stronger ability than Brass, Copper and S orientation in relieving stress within their monocrystals, which is consistent with the conclusions in Ref. [1].

The strong ability in relieving stress for Goss and Cube can also be well explained based on the Schmid's law. As we know, the Sch-

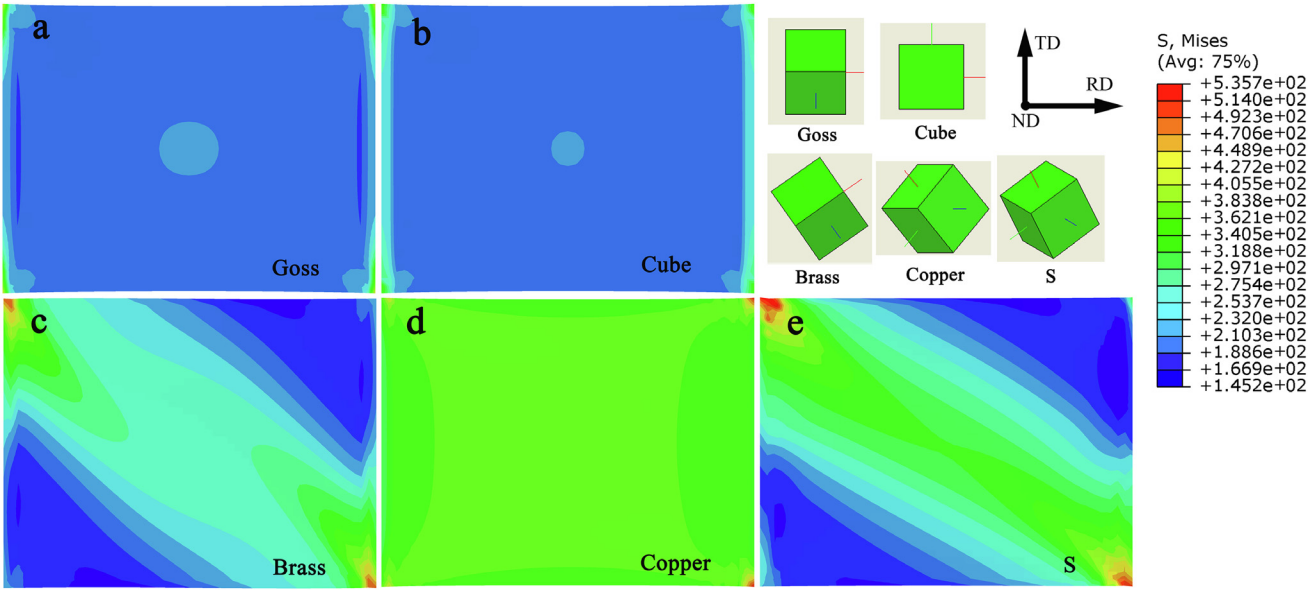

Fig. 5. The von Mises stress distribution within monocrystal for Goss (a), Cube (b), Brass (c), Copper (d), and S (e) grains after 3% deformation parallel with RD.

Table 2
The values of SF at 12 slip system of monocrystal for different orientation under RD loading.

Grain orientation	Slip plane and orientation												Max value	Initial slip system number
	(111)			$(11)\bar{1}$			$(11)\bar{1}$			$(11)\bar{1}$				
	$[10]\bar{1}$	$[10]\bar{1}$	$[01\bar{1}]$	$[10]\bar{1}$	[101]	[011]	[110]	$[10]\bar{1}$	[011]	[110]	[101]	$[01\bar{1}]$		
Goss (011) ⟨100⟩	0.408	0.408	0	0.408	0.408	0	0.408	0.408	0	−0.408	−0.408	0	0.408	8
Cube (001) ⟨100⟩	0.408	0.408	0	0.408	0.408	0	0.408	0.408	0	−0.408	−0.408	0	0.408	8
Brass (011) $\langle 2\bar{1}1 \rangle$	0.408	0.136	−0.272	0	0	0	0.272	0.272	0	−0.136	−0.408	0.272	0.408	2
Copper (112) $\langle \bar{1}\,\bar{1}1 \rangle$	0	0.272	0.272	0	0	0	−0.272	−0.272	0	−0.272	0	−0.272	0.272	6
S (213) $\langle \bar{3}\,\bar{6}4 \rangle$	−0.100	0.234	0.335	−0.261	−0.087	0.174	−0.422	−0.328	−0.094	−0.060	0.007	−0.067	0.422	1

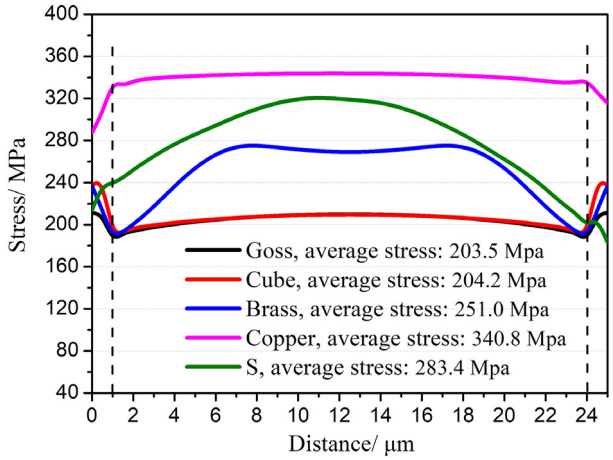

Fig. 6. The von Mises stress for different orientations along the red line in Fig. 1. (For interpretation of the references to color in this figure legend, the reader is referred to the web version of this article.)

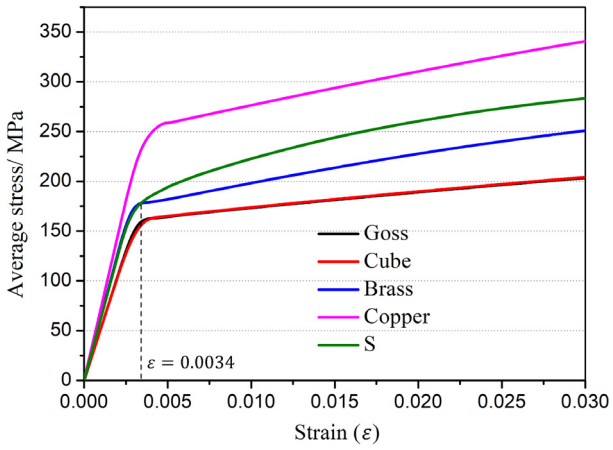

Fig. 7. Evolution of average stress during deformation for different orientations.

mid factor (SF) is the key for describing the magnitude in the resolved shear stress (τ^{α}). If the SF value of one crystal is low, then the τ^{α} of this crystal will also be low, making dislocation slipping difficult, and vice versa. Table 2 shows the values of SF for different orientations under RD loading. Firstly, it needs to be noted that there are 12 slip systems at one crystal and thereby there will be different SF values for different slip systems. Besides, if one SF is negative, then this SF is equivalent to its opposite value. It can be clearly seen from Table 2 that the maximum SF values of Goss and Cube are same, i.e. 0.408, and both numbers of maximum SF are also same, i.e. 8. Based on the application of Schmid law [56,57], the same SF values for these 8 slip systems signifies their τ^{α} values are also equal, which means that these 8 initial slip systems have equal potential to be simultaneously activated. The maximum SF value of Brass is also 0.408, but the number of EISS is only 2. This low EISS number is the reason for inducing relatively high stress at Brass crystal, as compared with Goss and Cube monocrystals. For Copper crystal, we can note that even the number of EISS reaches 6, more than 5, but the maximum value of SF value is only 0.272. Obviously, this low SF value is the main reason for inducing relatively high stress at Copper crystal. For S crystal, even though the maximum value of SF reaches 0.422, its number is only 1. In essence, the magnitude of stress formation is mainly dependent on not only the maximum value of SF, but also the number of participated initial slip system. Based on Ref. [11], the maximum and second maximum SF could provide a qualitative comparison in evaluating stress magnitude. A large second maximum SF will also be beneficial for the formation of low stress. For S crystal, the second maximum SF is only 0.335, below than Goss and Cube grains (0.408), and meanwhile its corresponding number is only 1. Even though we regard this second maximum slip system as a potential EISS, then the total number of EISS is only 2, far less than Goss and Cube grains. Therefore, the small number of EISS is a main reason contributing to high stress formation at S crystal. From the above analysis, it is also clear that as compared with Brass, Copper and S crystals, the larger SF value and higher number of EISS for Goss and Cube crystals principally contribute to the relatively low stress formation at Goss and Cube monocrystals.

On the other hand, based on maximum shear stress reference, we can put the values of SF for different slip systems on {1 1 1} pole figures to give more details about grain rotation in a way of dislocation slipping. Fig. 8 shows the simulated {1 1 1} pole figures of different crystals before and after deformation. The blue hyperbolas represent the maximum shear stress direction, making an angle of 45° with RD. Based on this reference, the maximum value of SF and its number (in parenthesis) for corresponding slip systems are shown in the pole figures. For Goss and Cube crystals, it can be observed that the SF values of 8 slip systems are the same, indicating that these 8 slip systems have equal ability to be activated at initial deformation stage. After deformation, the pole figures become scattered, which is attributed to grain rotation caused by dislocation slipping during deformation. Different from Cube grain, where all 8 slip systems could rotate around normal direction (ND), only 4 out of 8 slip systems in Goss grain could rotate around ND during deformation. Nevertheless, there is no obvious difference for Goss and Cube stress distribution. It also indicates that the change in grain rotation axes fail to have obvious influence on the magnitude of stress. For the Brass grain, only two slip systems with 0.408 SF value could be activated at initial deformation. This less EISS participation is the main reason responsible for relatively high stress within Brass crystal as compared with Goss and Cube. And it should also be noted that immobile slip systems with

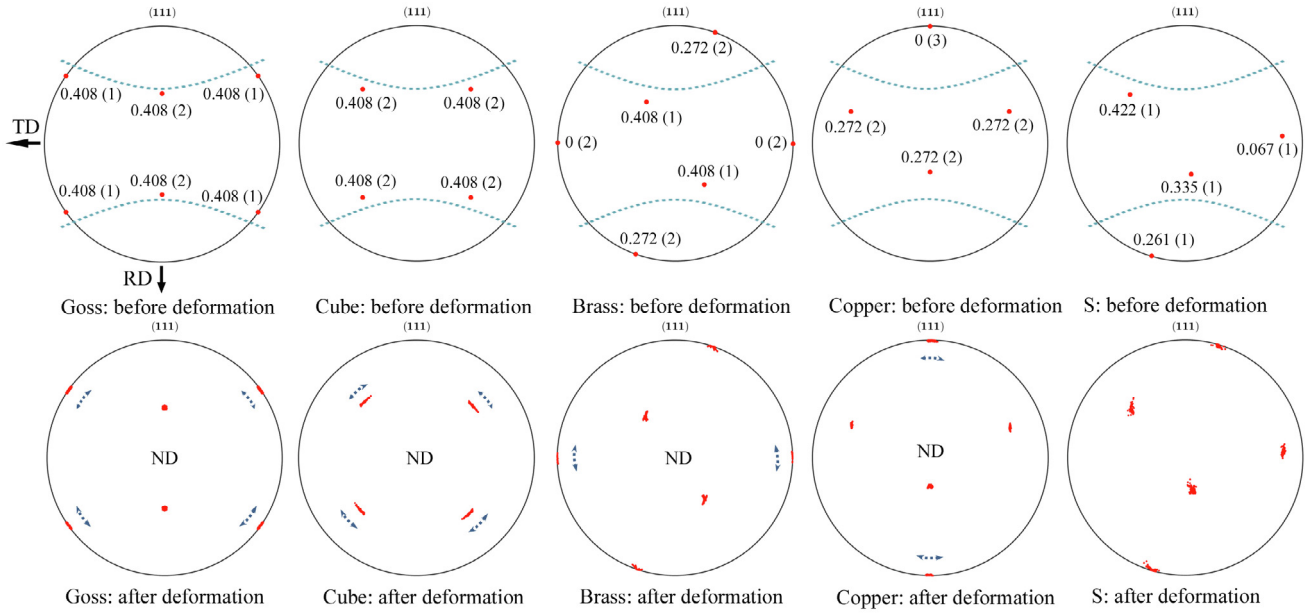

Fig. 8. The {1 1 1} pole figures of specific orientations before and after deformation.

SF value of 0 for Brass grain can also be activated after deformation. This is because the 4 {1 1 1} planes of these slip systems obviously rotate around ND during deformation. According to the simulation results of Wang et al., [20], the developed crystal rotations would change the resolved shear stress on slip systems and thus could make the hard slip systems with small SF values to be activated during deformation. This can also be confirmed by the In-situ EBSD observation of Chen et al. [11], who found that the "hard" slip system with SF value of 0 could gradually transform into relatively "soft" slip system during deformation. For Copper grain, although there are 8 slip systems having equal ability to be activated at initial deformation, the maximum value of SF is very low (0.272). Similarly, it can be observed that 3 immobile slip systems with SF value of 0 can also be activated after deformation. For S crystal, the initial activated slip system is only one, but other all slip systems can also be activated after deformation. Therefore, this confirms the assumption of present simulation that the 3% deformation can guarantee the activation of 12 system slips for all orientations. However, it should be realized that for the 3% deformation in monocrystals, the slip contribution to strain from lower SF is far less than that from the primary activated slip systems with maximum SF.

In order to further investigate the dependence of stress formation on SF and EISS, we change the load direction into parallel with TD, and corresponding simulation results are shown in Fig. 9. We can still observe that the stress distribution in Goss and Cube is symmetrical along both RD and TD, and similarly the stress distribution of Copper show symmetry only along RD direction. Brass and S fail to show symmetry along RD or TD direction. As it can be seen from Fig. 5, the crystal shape of Goss and Cube is symmetrical along both RD and TD directions, and that of Copper is symmetrical only along RD. Brass and S crystals fail to show any symmetry along RD or TD. Therefore, this further confirms that the crystal geometrical symmetry is positively correlated with the stress distribution symmetry. Fig. 8f gives a quantitative comparison for stress value along crystal midline parallel with TD. Similarly, due to the boundary condition effect, the great fluctuation of stress at two sides can be also observed. Interestingly, Cube crystal still shows the low stress, but comparatively the stress of Goss obviously becomes larger, reaching 232 MPa in average. This average stress of Goss is even higher than S and Copper. Besides, among the five orientations, Brass crystal produces the highest stress after deformation. Obviously, the change of stress formation is related to the change of SFs and EISS number when loading direction transforms from RD to TD. The SF values under TD loading are given in Table 3. Clearly, as compared with RD, the maximum value of SF and corresponding number for Cube crystal are still unchanged. However, for Goss grain, the number of EISS decreases to only 4, which is half of that under RD loading. Comparing with Cube crystal, this decrease in the number of maximum SF contributes to a corresponding increased stress within Goss. It is interesting to note that the maximum SF value and corresponding number of Brass grain is equal to that of Copper in Table 2, where the loading direction is parallel with RD. As expected, the average stress (340.8 MPa) of Brass under TD loading is almost equal to that of Copper under RD. This high stress formation is mainly due to the very low SF value (only 0.272). All in all, from the above simulation results in RD and TD, it is clear that the maximum SF value and the number of EISS play a predominated role in controlling the magnitude of internal stress within monocrystals.

3.2. Stress formation at bicrystal

In order to investigate stress formation in bicrystal model and how one crystal interacts with another, the stress simulation results for different grain boundary (GB) types are obtained. Fig. 10 shows the von Mises stress formation between Brass and other oriented grains at 3% strain when the loading direction is parallel with RD. Interestingly, there is no stress formation to be observed for the GBs between Goss and Brass or Cube and Brass grains. However, for other GBs between Brass and random grains, the obvious stress concentration at boundary is formed. This means that Cube and Goss grains are more favorable for reveling stress concentration at Goss-Brass and Cube-Brass GBs than other random GBs. Similar GB stress formation phenomena are also found when loading direction changes into parallel with TD (refer to the results of Fig. A1 in Appendix). In addition, Fig. 11 shows the relationship between GB stress and nominal strain (ε) for different bicrystals (take Goss-Brass, Cube-Brass, Grain 3-Brass, Grain 6-Brass, Grain 8-Brass and Grain10-Brass, as instances). It is clear

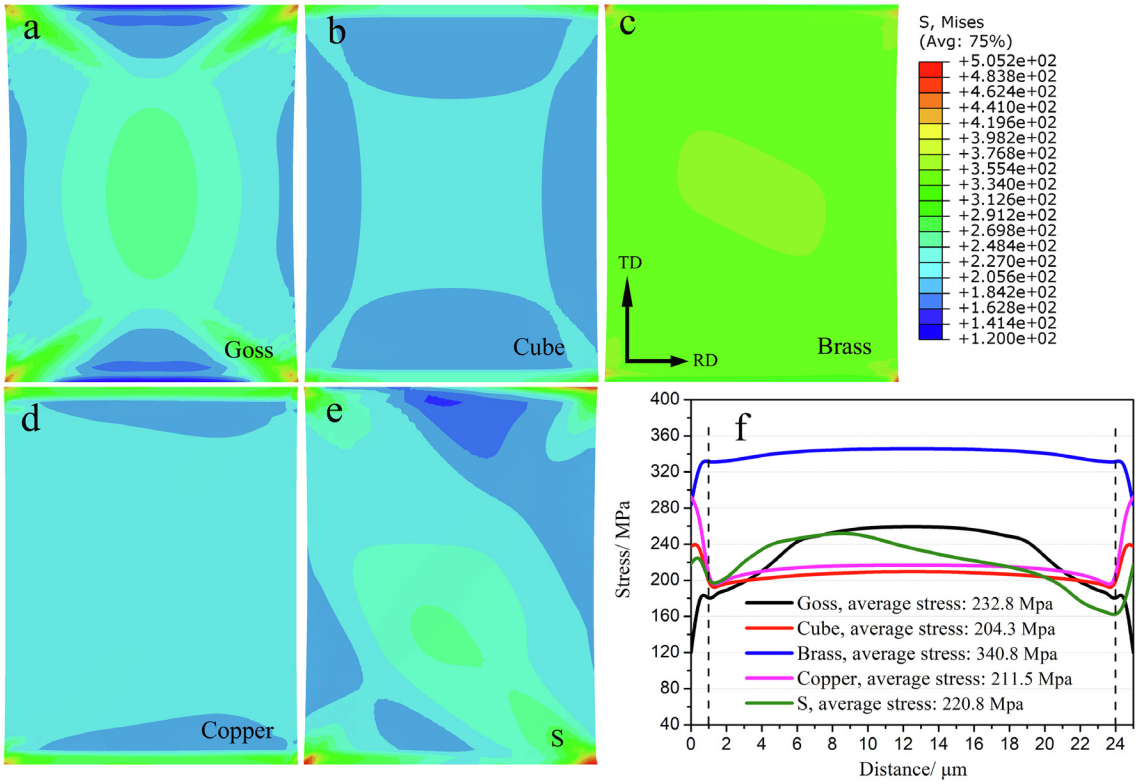

Fig. 9. The von Mises stress distribution for Goss (a), Cube (b), Brass (c), Copper (d) and S (e) after 3% deformation parallel with TD, and quantitative stress value (f) along crystal midline parallel with TD.

Table 3
The values of SF at 12 slip system of monocrystal for different orientation under TD loading.

Grain orientation	Slip plane and orientation-TD												Max value	Initial slip system number
	(111)			$(11\bar{1})$			$(1\bar{1}1)$			$(\bar{1}11)$				
	$[10\bar{1}]$	$[\bar{1}01]$	$[01\bar{1}]$	$[10\bar{1}]$	$[101]$	$[011]$	$[110]$	$[\bar{1}0\bar{1}]$	$[011]$	$[\bar{1}10]$	$[\bar{1}01]$	$[0\bar{1}1]$		
Goss $(011)\langle 100\rangle$	0	0	0	−0.408	−0.408	0	−0.408	−0.408	0	0	0	0	0.408	4
Cube $(001)\langle 100\rangle$	−0.408	0	0.408	−0.408	0	0.408	−0.408	0	−0.408	0.408	0	0.408	0.408	8
Brass $(011)\langle 2\bar{1}1\rangle$	0	0.272	0.272	0	0	0	−0.272	−0.272	0	−0.272	0	−0.272	0.272	6
Copper $(112)\langle\bar{1}\bar{1}1\rangle$	0	0	0	0	0	0	0	0.408	−0.408	0	−0.408	0.408	0.408	4
S $(213)\langle\bar{3}\bar{6}4\rangle$	−0.075	−0.059	0.015	0.261	0.087	−0.174	0.072	0.445	−0.373	−0.115	−0.298	0.184	0.445	1

that GB stress evolution for these bicrystals is similar and is consisted by two stages, corresponding to elastic and plastic deformations, respectively. For the elastic stage, the GB stress will gradually increase with increasing strain. When the strain reaches a certain value that corresponds to bicrystal yield point, bicrystals start to enter into the stage of plastic deformation, and the slope in GB stress increase with strain obviously decreases compared with elastic stage. By comparing GB stress for these bicrystals, the evolution of Goss-Brass and Cube-Brass GB stress is almost same during whole deformation, and their average GB stresses are always lower than other bicrystals (Grain 3-Brass, Grain 6-Brass, Grain 8-Brass, Grain 10-Brass). This further reveals that Cube and Goss grains are more favorable for reveling stress concentration at Goss-Brass and Cube-Brass GBs than other random GBs. Fig. 12 shows the GB stress formation between Copper and other oriented grains at 3% strain parallel with RD. In this case, we can observe that for all GBs obvious stress concentration exists, even for Goss-Copper and Cube-Copper boundaries. Fig. 13 shows the GB stress formation between S and other oriented grains at 3% strain parallel with RD. It is found that the stress concentration still exists at random grain participated GBs and even for Goss-S GB. However, for Cube-S GB, it is interesting to note that stress concentration at half of GB disappears. Compared with Goss grain, the disappearance of half GB stress concentration at Cube-S GB indicates that Cube has slightly stronger compatibility with S grain. The quantitative stress comparisons at 3% strain for different GBs are shown in Fig. 14. Clearly, for Brass-Goss and Brass-Cube, almost no stress concentration is formed at GBs and large stress concentration is found at Brass-random GBs. For Copper and S participated GBs, we can observe that the stress concentration exists at all GBs, even for Goss or Cube participated GBs. However, as compared with random grains, the stress formed at Goss or Cube GBs is obviously low. Therefore, it is concluded that Cube and Goss grains are more favorable for relieving stress concentration at GB than random grains. On top of that, another interesting observation is that despite the almost same monocrystal stress for Goss and Cube, Cube grain is relatively more favorable than Goss grain for reveling stress concentration at Copper and S participated GBs (Fig. 14c and

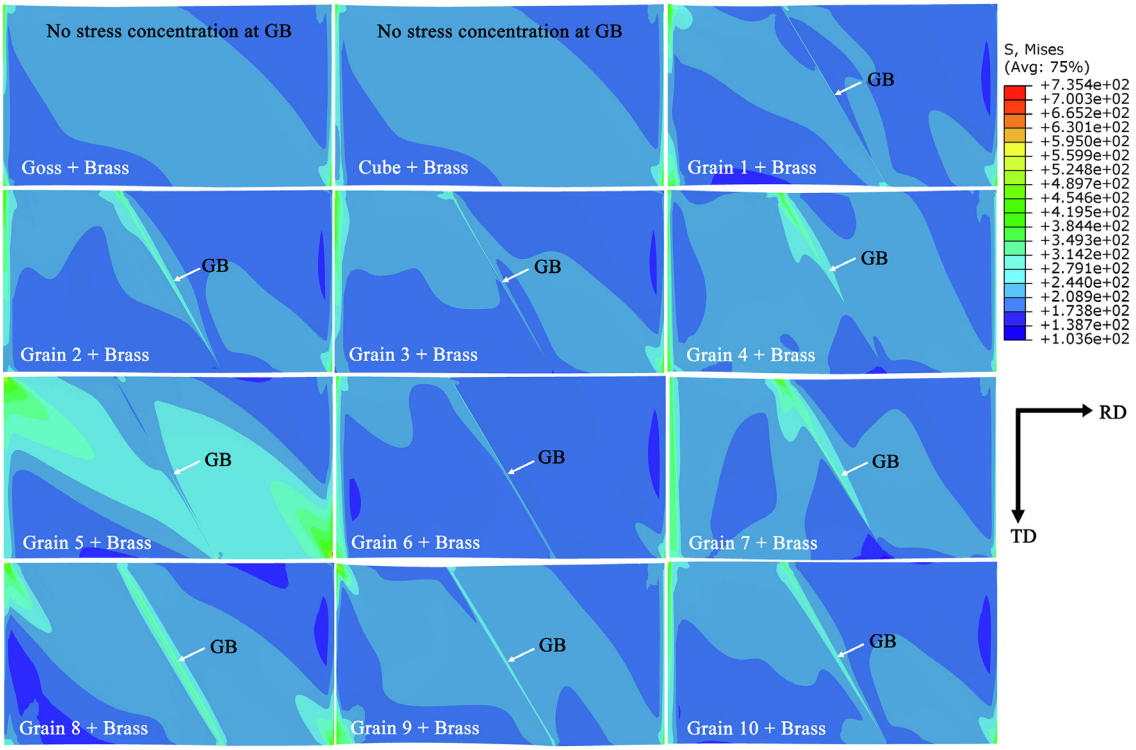

Fig. 10. The von Mises stress formation of GB between Brass and other oriented grains after 3% deformation parallel with RD.

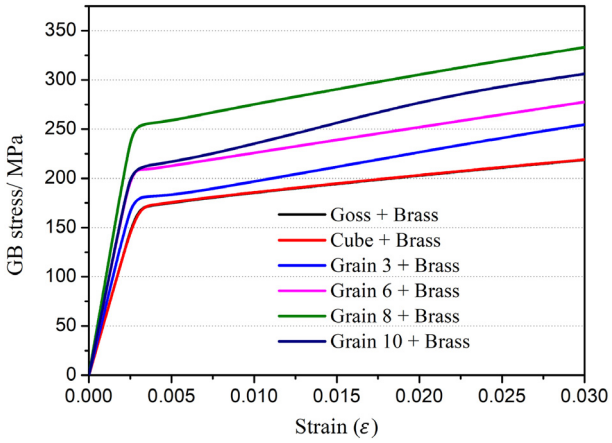

Fig. 11. Evolution of GB stress during deformation for different bicrystals.

e). Therefore, this means that the compatibility of Cube grain with deformed grains is slightly stronger than that of Goss grains. The present simulation result also provides an answer to the question why Cube texture is regarded as the best component for improving fatigue crack propagation resistance as reported in Ref. [58].

The low stress concentration at Cube or Goss participated GB leads us to reflect the correlation between the stress formed at GB and the stress formation in original monocrystal model. First in order to make a distinction between monocrystal and bicrystal terminology, the monocrystal is the terminology only used for original monocrystal model. Each crystal in bicrystal model is called as grain or crystal, rather than monocrystal. As we know, when loading direction is parallel with RD, the stress formed in Copper monocrystal is higher than that in S, and compared with S and Copper, the stress formed in Brass is the lowest (Fig. 5). Combining the results in Figs. 10, 12 and 13, it is indicated that the higher the stress formed in original monocrystal, the higher the stress formed in corresponding GB is. When the stress formed in a monocrystal is low, such as in case of Brass grain, then Goss and Cube grains have a good ability in relieving GB stress concentration with Brass (Fig. 10). When the stress formed in monocrystal is high, such as in case of Copper grain, Goss and Cube grains fail to effectively relieve stress concentration at GB (Fig. 12). This indicates that the high stress formed at each grain of bicrystal can transmit into GB, thereby contributing to a corresponding high stress at GB. Fig. 15 shows the change of simulated {1 1 1} pole figures for Goss-participated or Cube-participated bicrystals before and after deformation. Clearly after deformation, the {1 1 1} planes of Goss grain in Goss-Copper combination is more scattered than that in Goss-Brass and Cube-S bicrystals. In essence, the scattered degree of {1 1 1} planes is the reflection of dislocation slipping or grain rotation. The more scattered degree of Goss grain in Goss-Copper means that Goss needs larger dislocation slipping degree to relieve stress concentration than Goss-Brass and Goss-S combinations. As we know, the stress formed at Copper monocrystal is higher than Brass and S. This also indicates that when the stress formed at each grain of bicrystal is high, it can be transmitted into GB or another grain. This makes another grain in bicrystals needing larger degree of dislocation slipping to relieve this high stress or stress concentration. Besides, it is noted that the {1 1 1} planes of Cube in Cube-Brass and Cube-S bicrystals rotate around ND during deformation. However, the rotation axis in Cube grain of Cube-Copper combination not only includes ND, but also other axial directions, which indicates that the deformation of Cube grain is relatively more complex in Cube-Copper combination. This further confirms that when the stress formed at one grain of bicrystal is high, another grain will need more complex dislocation slipping behavior to relieve this high stress or stress concentration transmitted from its coterminous grain. Correspondingly, this complex dislocation slipping behavior also will lead to high stress or stress concentration at GB. However, this law is only satisfied for the

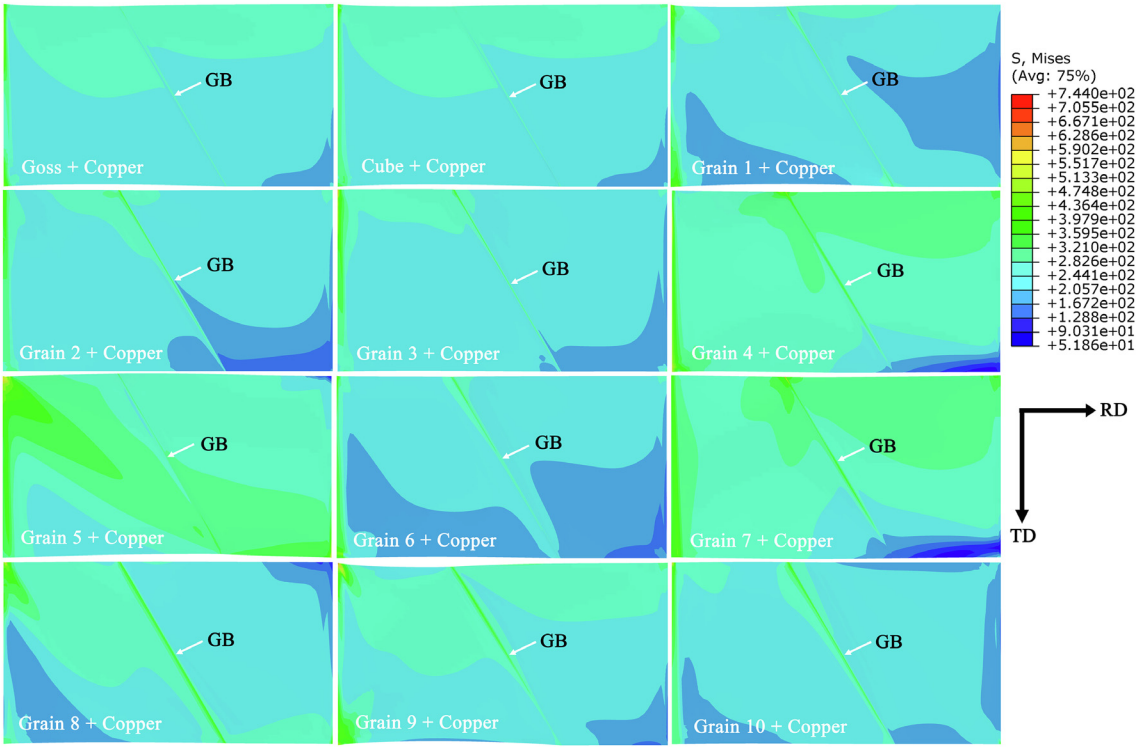

Fig. 12. The von Mises stress formation of GB between Copper and other oriented grains after 3% deformation parallel with RD.

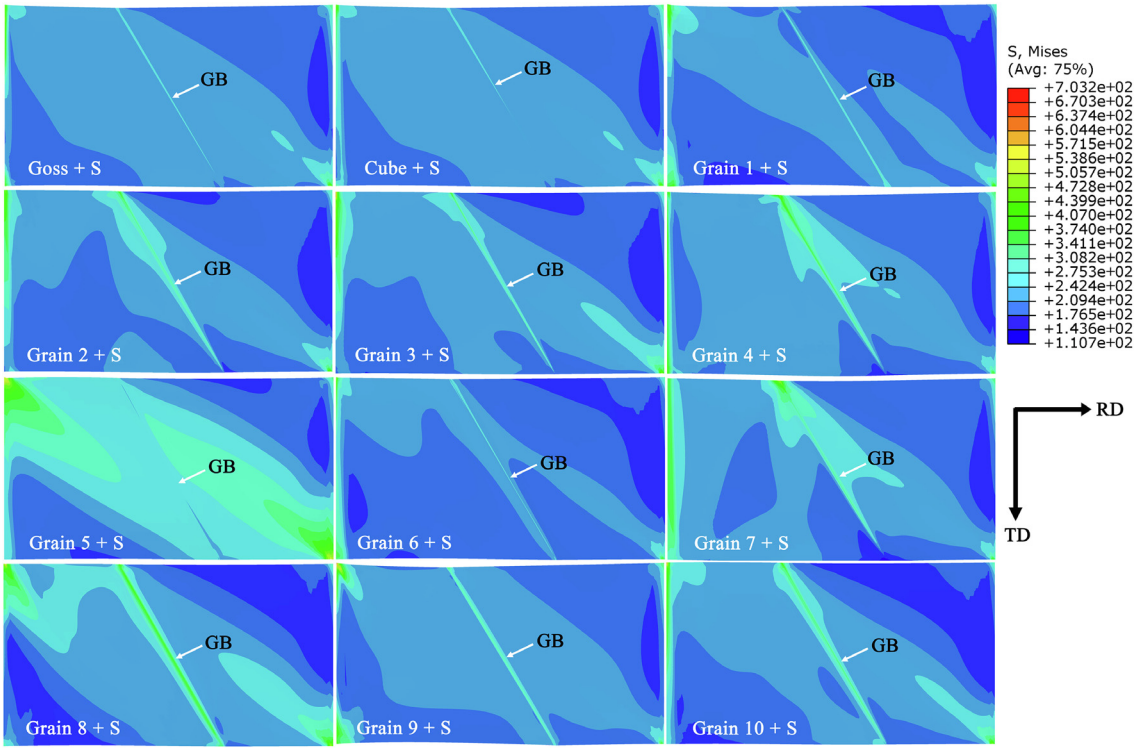

Fig. 13. The von Mises stress formation of GB between S and other oriented grains after 3% deformation parallel with RD.

bicrystal combinations between Goss and deformed components or Cube and deformed components, and is not satisfied to the combinations for random and deformed components. This can be confirmed by the simulation results in Fig. 16.

Fig. 16 shows the {1 1 1} pole figures of bicrystals between deformed orientations (Brass, Copper and S) and random orientations after 3% deformation under loading direction parallel with RD. The average stress in original monocrystal 6, 5 and 4 is calcu-

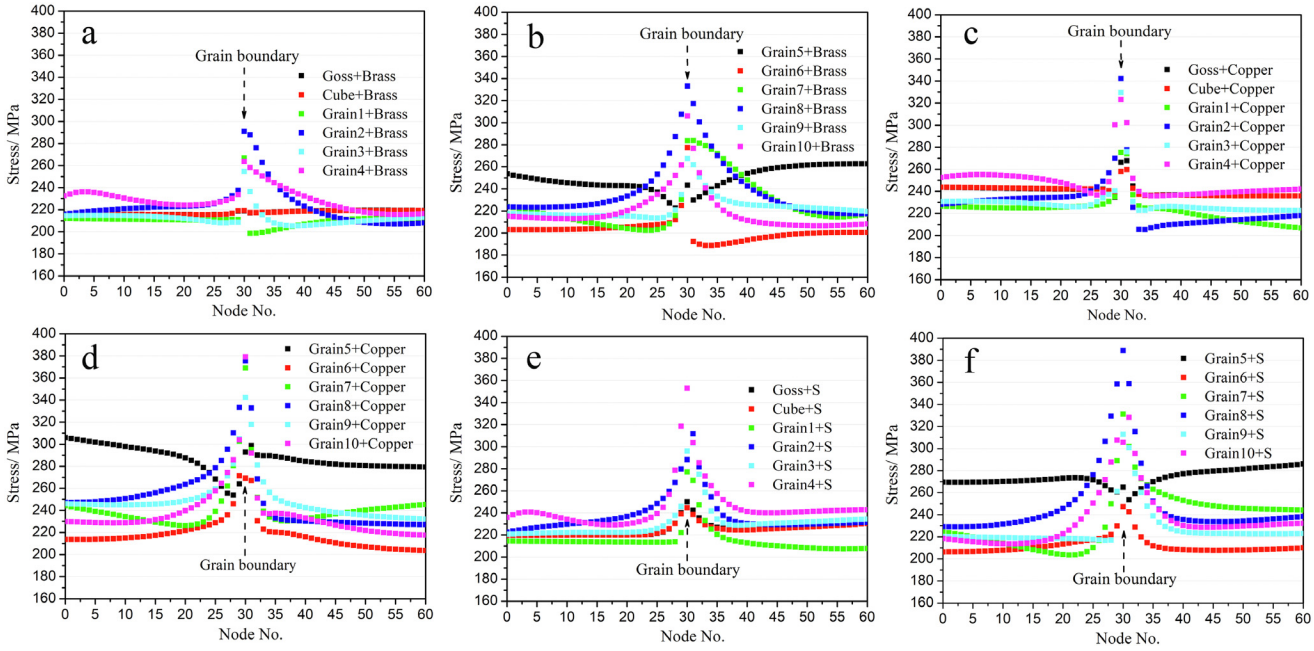

Fig. 14. The von Mises stress formation at Brass-participated (a and b), Copper-participated (c and d), and S-participated GBs (e and f).

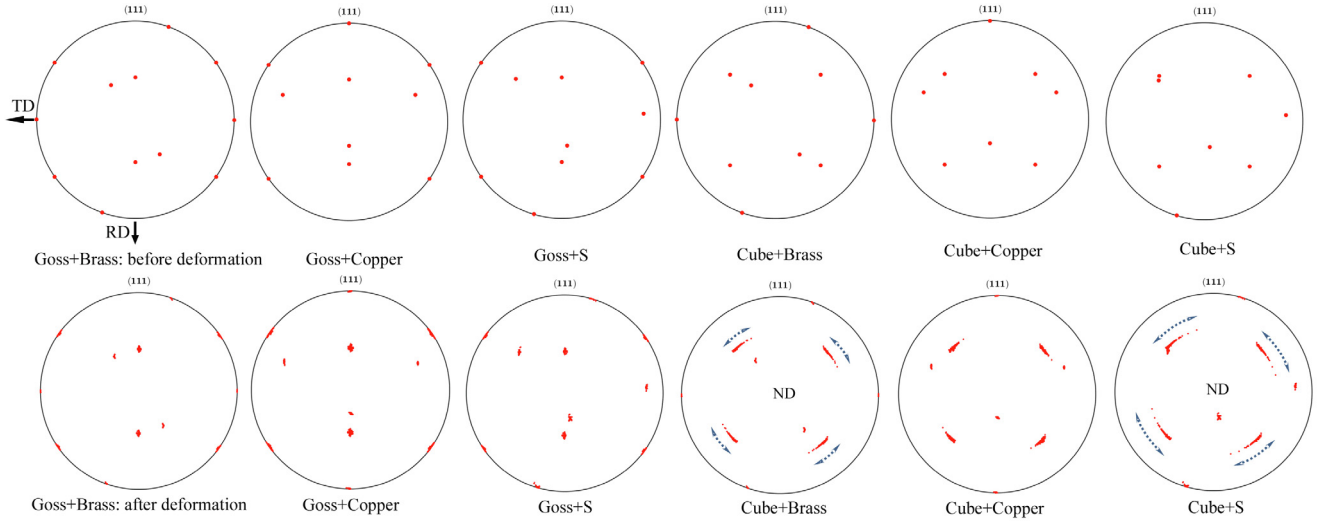

Fig. 15. The {1 1 1} pole figures of bicrystals between deformed orientations and Goss or Cube orientation before and after deformation under loading parallel with RD.

lated as 180.2, 290.9, 206.7 MPa, respectively. Obviously, as compared with grains 6 and 4, the higher stress within crystal 5 causes dislocation slipping or grain rotation in a larger degree when this grain gets interacted with these deformed grains of Brass, Copper or S. Theoretically, grain 5 will induce larger GB stress than grains 6 and 4. However, the GB stress for Grain 6-Brass, Grain 5-Brass, and Grain 4-Brass is 277.5, 243.5, 263.8 MPa, respectively. The high average stress in crystal 5 contrarily causes a relatively low stress concentration at GB. The GB stress for Grain 6-Copper, Grain 5-Copper, and Grain 4-Copper is 271.4, 298.7, 323.2 MPa, respectively. In this case, Grain 4 with the moderate average stress in monocrystal causes a very high stress concentration at GB. Similarly, this uncertain correlation is also found when the loading direction changes into parallel with TD (refer to the results of Fig. A2 in Appendix). Therefore, this leads us to suggest that the dislocation slip degree fails to have certain correlation with GB stress formation for the bicrystal types between random and deformed orientations. This also suggests that the stress formed at GB fails to have a certain correlation with dislocation density or internal stress of each monocrystal at bicrystal type, which is different from the mechanism of monocrystal stress formation.

Another interesting phenomenon needs to be noted is that the stress formed with Goss and Cube crystals is not the lowest in the bicrystal model (Fig. 14). Some random grains have lower stress within grain than Cube and Goss, such as grains 1 and 6. To the best of our knowledge, the stress distribution has complementary feature [59]. In other words, the low stress formed within crystal may be a result of stress relaxation at internal crystal due to forming high stress concentration at GB. Therefore, it raises a question whether this small stress within some random grain is caused by high stress concentration at GB or caused by their self-orientation feature. In order to answer this question, the simulated

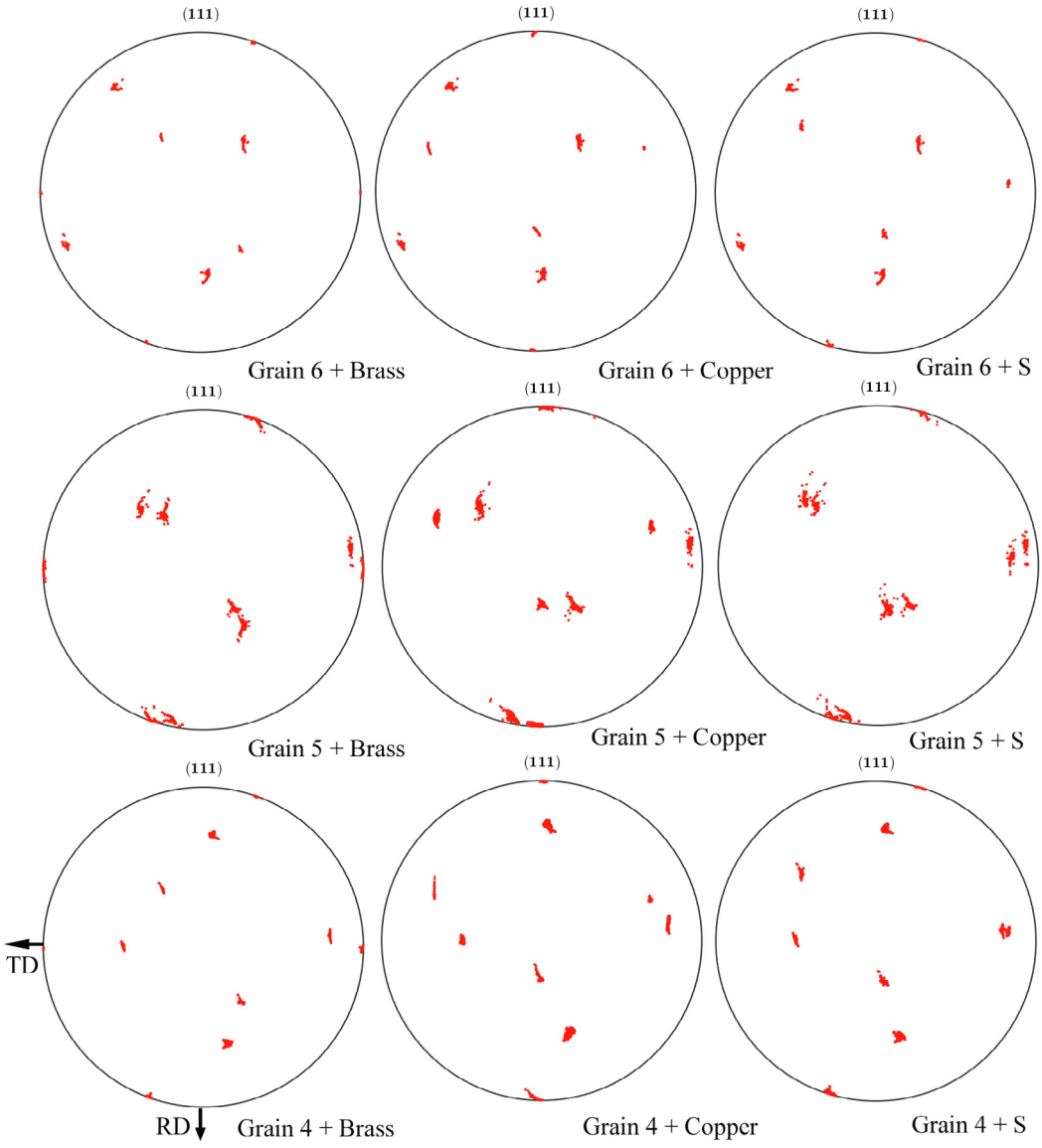

Fig. 16. The {111} pole figures of bicrystals between deformed orientations and random orientations after deformation under loading parallel with RD.

stress formation at monocrystal for some random grains is obtained, and the corresponding stress values along their crystal midlines are shown in Fig. 17. It can be observed that the average stress of grains 5 and 8 is obviously higher than Goss (203.5 MPa) and Cube (204.2 MPa) grains. The average stress of grain 4 is very close to Goss and Cube grains. Interestingly, the average stress of grains 1, 3 and 6 is lower than that of Goss and Cube. Clearly, this small stress within some random grains 1, 3 and 6 is not caused by high stress concentration at GB, but mainly by their self-orientation feature or self-SF characteristic. This further reveals that for monocrystal modelling, Goss and Cube are not the best orientations for relieving internal stress concentration. However, it should be noted that even though the average stress within grains 1, 3 and 6 is lower than Goss and Cube, the corresponding GB stresses caused by these orientations are higher than those caused by Goss and Cube (Fig. 14). The high stress formation at GBs caused by grains 1, 3 and 6 with low stress within crystals indicates that GB stress is not only dependent on self-grain stress character, but also on the compatibility between neighboring grains. This also further implies that Goss and Cube grains should have better compatibility with deformed grains than random grains.

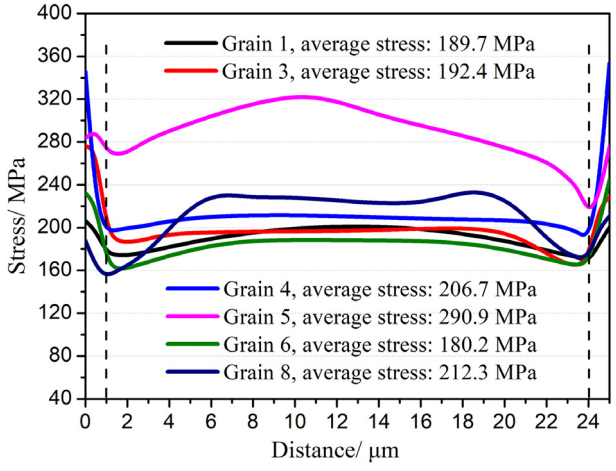

Fig. 17. The von Mises stress for random orientations along crystal midline parallel with RD.

3.3. Correlation factors for GB stress

From the above numerical results, it is clear that the stress formation at grain boundary (GB) is very complex. The magnitude of stress must be affected by the compatibility between two neighboring grains. Actually, Luster et al. [6] first proposed the geometric compatibility factor (GCF) to describe the compatible ability among grains in Ti-Al alloys. Specifically, for two adjacent grains with a slip system pair, the GCF can be expressed as the magnitude of $\cos\lambda \times \cos\phi$. Where λ is the angle between the two slip directions for this system pair, and ϕ is the angle between the two slip plane normals. For hexagonal close-packed (HCP) Ti-Al alloys, there are $3 \times 3 = 9$ possible slip system pairs; for face-centered Cubic (FCC) structure, there are $12 \times 12 = 144$ possible slip system pairs. It is regarded that of all slip system pairs, the slip system pair with the highest GCF would be easiest to be active. Therefore, in present work, we use the maximum geometric compatibility factor (m_{ab}) to represent the compatible ability between two conterminous grains a and b, and it can be expressed as:

$$m_{ab} = \max(\cos\lambda \times \cos\phi) \tag{33}$$

Recently, Sun et al. [7] further put forward one comprehensive factor (M_k) combining the maximum Schmid factor product (SF_{ab}) and m_{ab} in magnesium alloys, which is expressed as:

$$M_k = \max(k_a) \cdot m_{ab} \cdot \max(k_b) \tag{34}$$

where $\max(k_a)$ and $\max(k_b)$ represent the maximum Schmid factor (SF) values of slip system corresponding to grains a and b, respectively. It is suggested that the higher the M_k, the stronger the deformation compatibility between two conterminous grains is. However, the above Eqs. (33) and (34) are proposed for titanium and magnesium alloys. The crystal structure of titanium and magnesium alloys is hexagonal close-packed (HCP). Compared with 2024 aluminum alloys with face-centered Cubic (FCC) structure, the slip system in HCP alloys is only one fourth of aluminum alloys. Therefore, it also indicates that the compatible deformation behavior in aluminum alloys is different from titanium or magnesium alloys. It is further analyzed in the present work that whether the two factors proposed in Eqs. (33) and (34) are also suitable for describing the deformation character or stress formation at GB. Besides, we use Pearson correlation coefficient (r) to quantify the strength of correlation between SF_{ab},m_{ab}, M_k and GB stress, which can be expressed as [60]:

$$r = \frac{\sum_{i=1}^{n}\left(X_i - \bar{X}\right)\left(Y_i - \bar{Y}\right)}{\sqrt{\sum_{i=1}^{n}\left(X_i - \bar{X}\right)^2}\sqrt{\sum_{i=1}^{n}\left(Y_i - \bar{Y}\right)^2}} \tag{35}$$

where X equals to SF_{ab},m_{ab} or M_k, and Y equals to the boundary stress. The Pearson correlation coefficient is a measurement of linear correlation between two variables X and Y. It has a value in the range from −1 to +1, where −1 is for 'total negative linear correlation', +1 is for 'total positive linear correlation', and 0 is 'no linear correlation'. The dependence between stress formation and SF_{ab},m_{ab} or M_k, and the corresponding Pearson correlation coefficients are shown in Fig. 18. First, it is observed that in any cases, the Pearson correlation coefficient (r) for M_k is almost always higher than m_{ab}, indicating that M_k shows higher dependence than m_{ab} on GB stress. As a result, M_k is more accurate factor for describing the compatible deformation ability than m_{ab}. Besides, it is found that the dependence between stress formation and SF_{ab},m_{ab} or M_k changes for different GBs. When the loading direction is parallel to RD, SF_{ab} shows a higher dependence than m_{ab} or M_k with boundary stress for Brass participated GBs (Fig. 18a-c). In this case, the Pearson correlation coefficient (r) for SF_{ab} reaches 0.761. However, when the loading direction is parallel to TD, M_k shows a higher dependence than SF_{ab} or m_{ab} on GB stress (Fig. 18d-f). Interestingly for Copper participated boundary, the r for M_k is very high, reaching 0.794 (Fig. 18i). However, for S participated boundaries, the corresponding r forM_k is almost close to 0, indicating M_k is almost no linear correlation with boundary stress (Fig. 18l). Instead, a relatively good dependence (r = 0.348) between SF_{ab} and boundary stress is found (Fig. 18k). From the results, it is clear that the strong correlation between M_k and GB stress in HCP crystals is not always suitable in AA2024 alloy with FCC structure, which is consistent with the experimental results in Ref. [61]. In HCP crystals, the number of slip system is 3, and the activated slip system is only 1 during deformation. In this case, the cross slipping is difficult to occur. However, in FCC structure, the number of slip system reaches 12, and much cross slipping can occur especially when the equivalent initial slip system (EISS) is higher than 1. Therefore, it is suggested that the different dislocation slip mechanisms between FCC and HCP crystals lead to the inapplicability of dependence relation between M_k and GB stress for FCC crystal. As we understand,M_k is the corresponding largest value among all slip system pairs. At HCP crystals, it is reasonable to use M_k to represent overall deformation behavior because the activated slip system is only 1. However, in FCC crystal structure, M_k cannot always reasonably represent the overall deformation behavior at GB. For example, for S GBs, the EISS is only 1 (see Table 2), but other slip systems with lower SF values can also be activated (Fig. 8), which will make these slip systems also interacted with neighboring grains during deformation. Obviously in this case, M_k cannot reasonably represent the overall interaction behavior of slip system pairs at GB. As a result, the r for M_k is almost close to 0 (Fig. 18l), indicating no linear correlation between M_k and GB stress. With the increase in the number of EISS, M_k can be gradually reasonable to represent the interaction behavior for slip system pairs at two coterminous grains. As it can be seen in Fig. 18a-c, the EISS for Brass grain increases to 2, the r for M_k increases to 0.399. When the EISS for Brass grain reaches 6 by changing loading direction into parallel TD, the r for M_k increases to 0.504 (Fig. 18d-f). Similarly, a large r (0.794) for M_k is also observed for Copper grain in which the EISS is 6 (Fig. 18g-i). Therefore, it is clear that the comprehensive factor (M_k) shows the improved dependence with GB stress when the number of EISS is increased. This also leads us to suggest that GB interaction behavior is controlled by more than one geometric compatibility factor (GCF) or slip system pair, and it is necessary in FCC crystals to consider other GCFs effect caused by other activated slip systems. Based on von Mises Criterion, it is known in FCC crystals that 5 out of 12 independent slip systems are needed to guarantee compatible deformation at GBs [62,63]. As a result, each 5 independent slip systems in two coterminous grains will also form 25 different slip pairs or 5 GCFs (one independent slip system produces one GCF). However, it should be noted that these 5 independent slip systems are not only confined to the slip systems with 5 largest SF values, but any 5 slip systems out of 12. So, it will produce $12 \times 12 = 144$ possible slip pairs or 12 GCFs between two coterminous grains. But, only 5 of 12 GCFs are actually activated during GB interaction behavior. In light of this, a modified quantitative correlation between GB stress and a new comprehensive factor (M_k') is further proposed for more accurately describing GB interaction behavior of AA 2024 FCC crystal. After considering the contribution from 5 independent slip systems at GB interaction, the new geometric compatibility factor (m_{ab}') between two coterminous grains a and b can be expressed as:

$$m_{ab}' = \frac{\sum_{i=1}^{5} m_{abi}}{5} \tag{36}$$

where m_{abi} represents the i^{th} maximum GCF out of all 12 GCFs between grains a and b. Besides, in any case we can observe that SF_{ab} always show a positive linear correlation with boundary stress

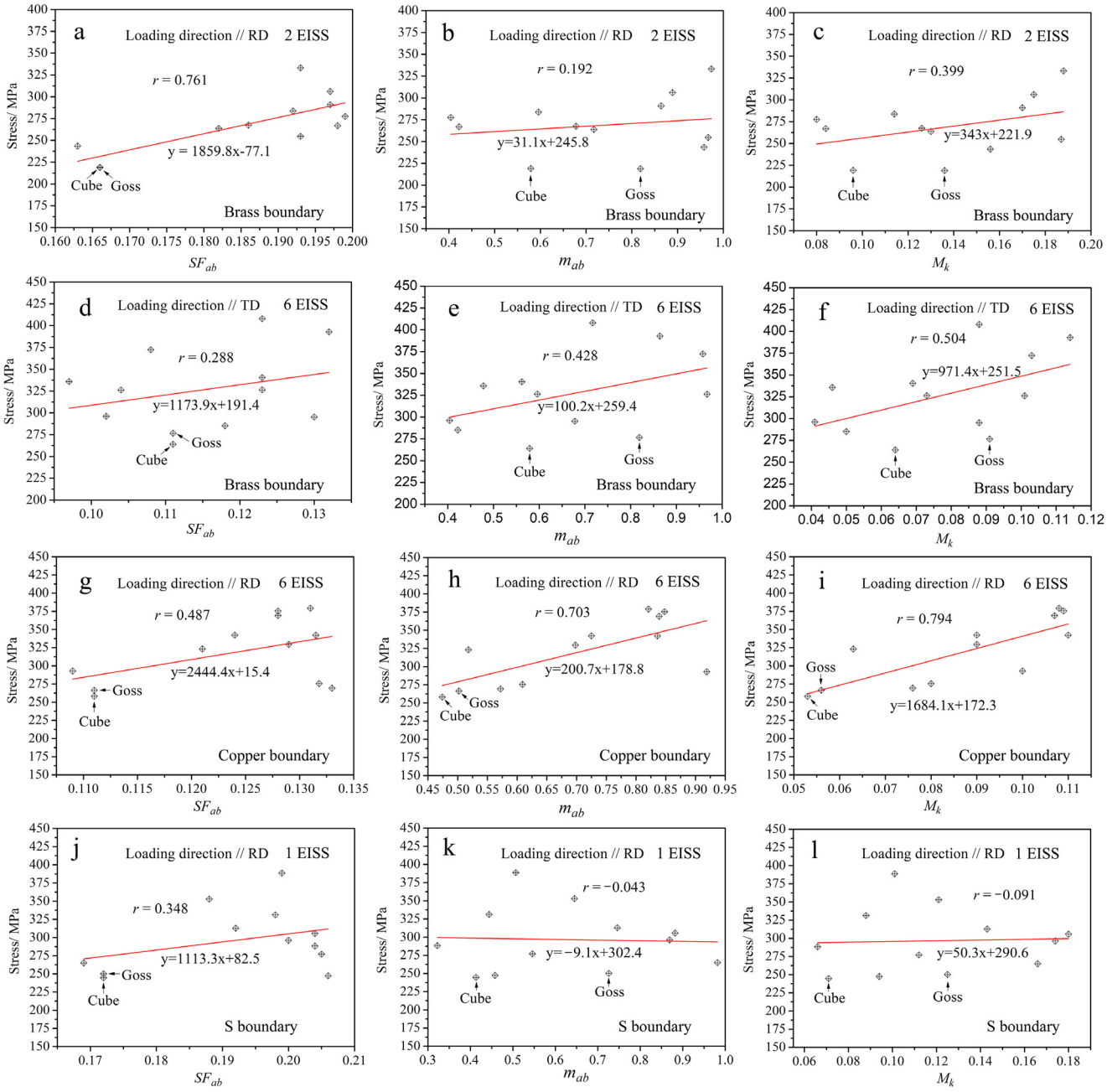

Fig. 18. The dependence between GB stress and maximum SF product (SF_{ab}), geometry compatibility factor (m_{ab}) or the factor (M_k) combining SF_{ab} with m_{ab}. The loading direction is parallel to RD for a-c and g-l, and the loading direction is parallel to TD for d-f.

(Fig. 18). This also indicates that high SF_{ab} is generally beneficial for the formation of high GB stress. It is worthy to realize that although all slip systems are activated in 3% deformation in the present work, those slip systems with large SF values still play a predominated role in affecting GB stress formation. Therefore, considering the dominated role played by maximum SF values, the SF product doesn't need to be changed with its old one (SF_{ab}). Actually, if we use the average value of the 5 maximum SFs, it is found that the averaged 5 maximum SF values will reduce the role played by the maximum SF value. As a result, the accuracy in describing GB interaction behavior of AA 2024 FCC crystal will be decreased. As a result, the old SF_{ab} will still be used for the present FCC crystal. Then, the new comprehensive factor ($M_k{}'$) is the product of SF_{ab} and $m_{ab}{}'$, and can be written as:

$$M_k{}' = \max(k_a) \times \frac{\sum_{i=1}^{5} m_{abi}}{5} \times \max(k_b) \tag{37}$$

where m_{abi} represents the i^{th} maximum geometric compatibility factor between grains a and b. $\max(k_a)$ and $\max(k_b)$ represent the maximum SF values of slip system corresponding to grains a and b, respectively. The dependence between GB stress formation and $M_k{}'$, and the corresponding Pearson correlation coefficients are shown in Fig. 19. It is clear that after considering the contribution from 5 independent slip systems, the Pearson correlation coefficient (r) increases and reaches a relatively large value. The r values in Fig. 19a-c are very close to 1, which means that the stress at GB satisfies an almost total positive linear correlation with this new comprehensive factor ($M_k{}'$). Although, the r value in Fig. 19d is relatively

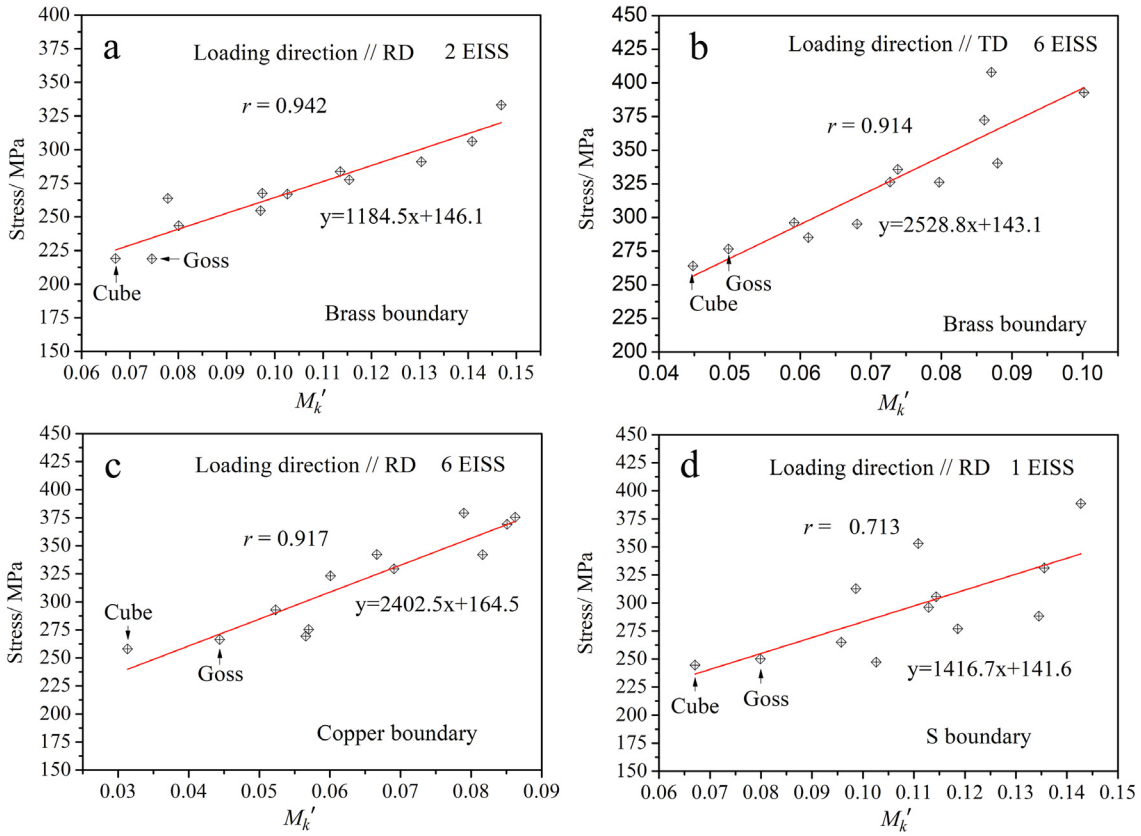

Fig. 19. The dependence analyses between GB stress and the new comprehensive factor (M_k'), a and b are Brass boundary, and c and d are Copper and S boundaries, respectively.

small, 0.713, its increasing amplitude is the largest one considering the original r value is close to 0 (Fig. 18l). From the above analyses, it is clear that the proposed new comprehensive factor (M_k') considering the contribution from 5 to independent slip system criterion effectively improves its dependence with the GB stress formation.

4. Conclusion

We investigated stress formation of monocrystal and bicrystals in specific oriented grains or grain boundaries of AA2024 alloy by the use of orientation component Crystal Plasticity Finite Element Method. The main conclusions are:

(1) The maximum SF value and the number of EISS play a main role in controlling the magnitude of internal stress at monocrystals. When loading direction is parallel with RD, as comparison with Brass, Copper and S monocrystals, the larger SF value and higher number of EISS for Goss and Cube crystals principally contributes to the relatively lower stress formation within their monocrystals.
(2) There is no positive relation between the stress formed within monocrystal and the corresponding induced GB stress at bicrystal model. Compared with random grains, Goss and Cube grains are not the best ones for relieving stress concentration caused by their orientation feature, but they are the best two ones for relieving GB stress concentration at bicrystal model.
(3) The dependence law between GB stress and the comprehensive factor (M_k) as proposed in HCP crystal is not always suitable for FCC AA2024 alloy. Comparatively with old comprehensive factor (M_k), the new comprehensive factor (M_k') merging the contribution from 5 to independent slip system criterion shows an improved positive linear correlation with GB stress.

Declaration of Competing Interest

The authors declare that they have no known competing financial interests or personal relationships that could have appeared to influence the work reported in this paper.

Acknowledgements

The authors are grateful for the financial support from National Natural Science Foundation of China (51901073), China Scholarship Council (201808420393), and PhD Research Startup Foundation of Hubei University of Automotive Technology (BK201702).

Appendix. GB stress formation under loading parallel to TD

Fig. A1 shows the GB stress formation for Brass participated bicrystal model and quantitative comparison for different GB stress when the loading direction is parallel to TD. We can see that there is no obvious stress concentration at Goss-Brass boundary. However, slight stress concentration is observed at Cube-Brass boundary. Nevertheless, the stress at Cube-Brass boundary is still lower than that at Goss-Brass boundary. On top of that, it is observed that as compared with random-Brass boundaries, Goss and Cube still have stronger ability in relieving GB stress concentration. Fig. A2 provides the data about the effect of stress formed by original monocrystal on dislocation slipping degree under loading with

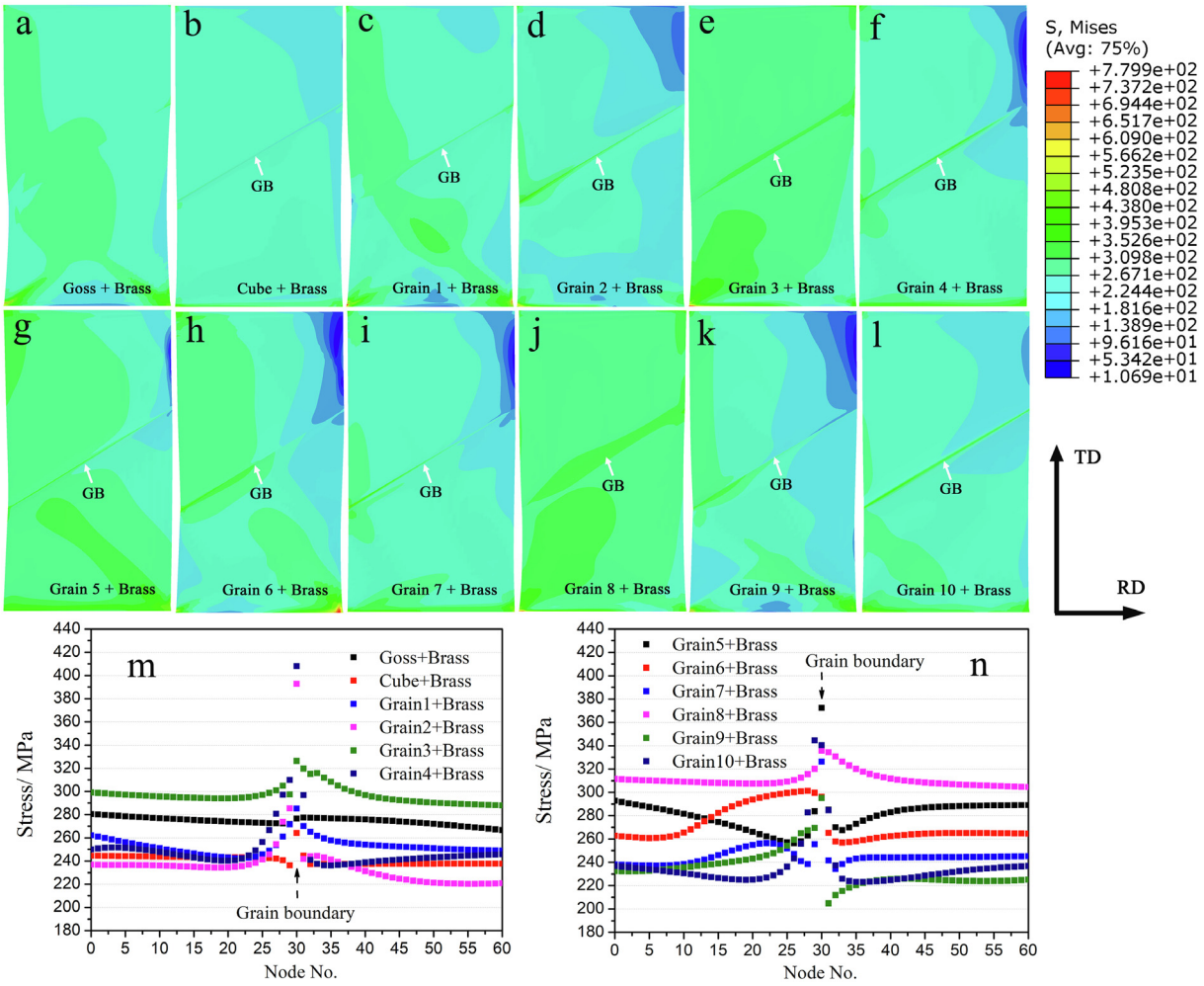

Fig. A1. The stress formation (a-l) of GBs between Brass and other oriented grains under loading parallel with TD and quantitative comparison (m and n) for different GB stress.

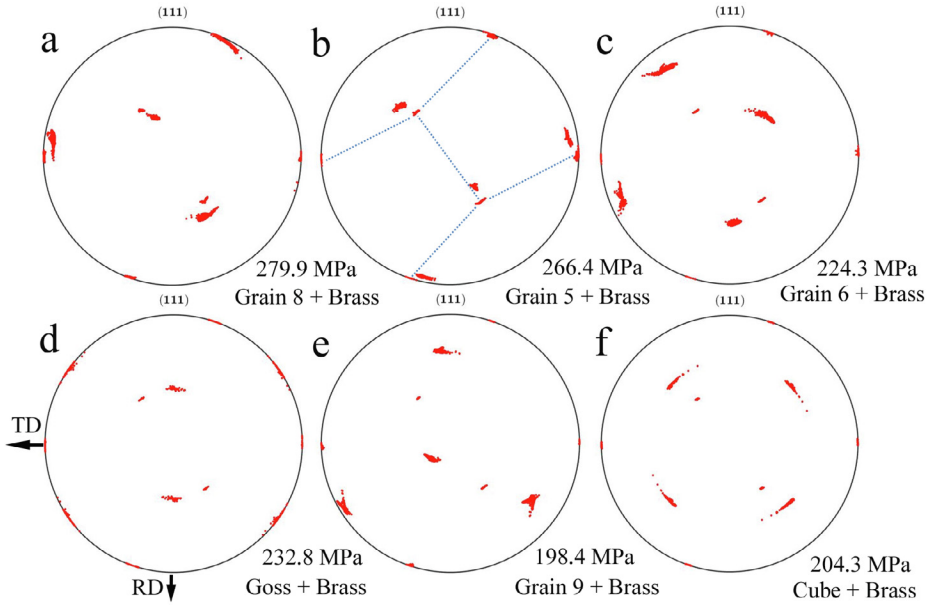

Fig. A2. The {111} pole figures of bicrystals between Brass and random orientations under loading parallel with TD.

TD (take Brass participated bicrystal model as example). It can be seen that for random grain, with the decrease of self-stress within original monocrystal, the scattering degree for {1 1 1} planes of Brass gradually decreases. This indicates that when the stress formed at one grain of bicrystal is high, larger degree in dislocation slipping behavior for another conterminous grain is needed to relieve stress or stress concentration. However, this law is not suitable for Goss and Cube grain, which is essentially attributed to the different symmetry feature among Goss, Cube and other random orientations. Also, for random grain, this large degree in dislocation slipping does not necessarily lead to high stress concentration at GB. For example, the stress with crystal 8 is 279.9 MPa that is higher than that in crystal 5 (266.4 MPa). However, the stress at Grain 8-Brass boundary is 335.8 MPa that is lower than the stress (372.3 MPa) at Grain 5-Brass boundary. It also further confirms that the stress formed at original monocrystal fails to have positive relation with the stress at corresponding GB. That is to say, there is no strict correlation between dislocation slipping degree and GB stress.

References

[1] Z.Y. Liu, F.D. Li, P. Xia, S. Bai, Y.X. Gu, D.E. Yu, S.M. Zeng, Mechanisms for Goss-grains induced crack deflection and enhanced fatigue crack propagation resistance in fatigue stage II of an AA2524 alloy, Mater. Sci. Eng. A 625 (2015) 271–277.

[2] F.D. Li, Z.Y. Liu, W.T. Wu, P. Xia, P.Y. Ying, Q. Zhao, J.L. Li, S. Bai, C.W. Ye, On the role of texture in governing fatigue crack propagation behavior of 2524 aluminum alloy, Mater. Sci. Eng. A 669 (2016) 367–378.

[3] F.D. Li, Z.Y. Liu, W.T. Wu, Q. Zhao, Y.R. Zhou, S. Bai, X.H. Wang, G.H. Fan, Slip band formation in plastic deformation zone at crack tip in fatigue stage II of 2xxx aluminum alloys, Int. J. Fatigue 91 (2016) 68–78.

[4] T.R. Bieler, P. Eisenlohr, F. Roters, D. Kumar, D.E. Mason, M.A. Crimp, D. Raabe, The role of heterogeneous deformation on damage nucleation at grain boundaries in single phase metals, Int. J. Plasticity 25 (2009) 1655–1683.

[5] H. Pouriayevali, B.X. Xu, Decomposition of dislocation densities at grain boundary in a finite-deformation gradient crystal-plasticity framework, Int. J. Plasticity 96 (2017) 36–55.

[6] J. Luster, M.A. Morris, Compatibility of deformation in two-phase Ti-Al alloys: dependence on microstructure and orientation relationships, Metall. Mater. Trans. A 26A (1995) 1745–1756.

[7] J. Sun, L. Jin, J. Dong, F. Wang, S. Dong, W. Ding, A.A. Luo, Towards high ductility in magnesium alloys - the role of intergranular deformation, Int. J. Plasticity 123 (2019) 121–132.

[8] C.S. Hyun, M.S. Kim, S.-H. Choi, K.S. Shin, Crystal plasticity FEM study of twinning and slip in a Mg single crystal by Erichsen test, Acta Mater. 156 (2018) 342–355.

[9] M. Sachtleber, Z. Zhao, D. Raabe, Experimental investigation of plastic grain interaction, Mater. Sci. Eng. A 336 (2002) 81–87.

[10] N. Zhang, W. Tong, An experimental study on grain deformation and interactions in an Al-0.5%Mg multicrystal, Int. J. Plasticity 20 (2004) 523–542.

[11] P. Chen, S.C. Mao, Y. Liu, F. Wang, Y.F. Zhang, Z. Zhang, X.D. Han, In-situ EBSD study of the active slip systems and lattice rotation behavior of surface grains in aluminum alloy during tensile deformation, Mater. Sci. Eng. A 580 (2013) 114–124.

[12] S. Groh, E.B. Marin, M.F. Horstemeyer, H.M. Zbib, Multiscale modeling of the plasticity in an aluminium single crystal, Int. J. Plasticity 25 (2009) 1456–1473.

[13] V. Dupont, F. Sansoz, Molecular dynamics study of crystal plasticity during nanoindentation in Ni nanowires, J. Materials Res. 24 (2009) 948–956.

[14] K. Zhang, K. Marthinsen, B. Holmedal, T. Aukrust, A. Segatori, Coupled FEM and Alamel-type polycrystal plasticity modelling applied to extrusion of aluminium alloys, Mater. Today: Proc. 2 (2015) 4898–4903.

[15] V. Tari, A.D. Rollett, H.E. Kadiri, H. Beladi, A.L. Oppedal, R.L. King, The effect of deformation twinning on stress localization in a three dimensional TWIP steel microstructure, Modelling Simul. Mater. Sci. Eng. 23 (2015) 045010.

[16] K. Zhang, K. Marthinsen, B. Holmedal, T. Aukrust, A. Segatori, Through thickness variations of deformation texture in round profile extrusions of 6063-type aluminium alloy: experiments, FEM and crystal plasticity modelling, Mater. Sci. Eng. A 722 (2018) 20–29.

[17] D. Kishi, T. Mayama, Y. Mine, K. Takashima, Crystallographic study of plasticity and grain boundary separation in FeCo alloy using small single- and bi-crystalline specimens, Scripta Mater. 142 (2018) 1–5.

[18] M. Kuroda, V. Tvergaard, Effects of texture on shear band formation in plane strain tension/compression and bending, Int. J. Plasticity 23 (2007) 244–272.

[19] Z. Zhao, S. Kuchnicki, R. Radovitzky, A. Cuitino, Influence of in-grain mesh resolution on the prediction of deformation textures in fcc polycrystals by crystal plasticity FEM, Acta Mater. 55 (2007) 2361–2373.

[20] H. Wang, C. Lu, K. Tieu, A crystal plasticity FEM investigation of a Cu single crystal processed by accumulative roll-bonding, J. Mater. Res. Technol. 8 (2019) 5057–5065.

[21] H. Lim, C.C. Battaile, J.E. Bishop, J.W. Foulk III, Investigating mesh sensitivity and polycrystalline RVEs in crystal plasticity finite element simulations, Int. J. Plasticity 121 (2019) 101–115.

[22] Y. Zhou, Q.B. Fan, X. Liu, D.D. Wang, X.J. Zhu, Experimental study and crystal plasticity finite element simulations of nano-indentation-induced lattice rotation and the underlying mechanism in TC6 single α-grain, Mater. Des. 188 (2020) 108423.

[23] A. Ma, F. Roters, D. Raabe, On the consideration of interactions between dislocations and grain boundaries in crystal plasticity finite element modeling –Theory, experiments, and simulations, Acta Mater. 54 (2006) 2181–2194.

[24] A.K. Kanjarla, P. Van Houtte, L. Delannay, Assessment of plastic heterogeneity in grain interaction models using crystal plasticity finite element method, Int. J. Plasticity 26 (2010) 1220–1233.

[25] P. Van Houtte, L. Delannay, S.R. Kalidindi, Comparison of two grain interaction models for polycrystal plasticity and deformation texture prediction, Int. J. Plasticity 18 (2002) 359–377.

[26] I. Benedetti, V. Gulizzi, V. Mallardo, A grain boundary formulation for crystal plasticity, Int. J. Plasticity 83 (2016) 202–224.

[27] T.L. Cheng, Y.H. Wen, J.A. Hawk, Diffuse interface approach to modeling crystal plasticity with accommodation of grain boundary sliding, Int. J. Plasticity 114 (2019) 106–125.

[28] Q. Zhao, Z.Y. Liu, M. Abdel Wahab, Enhanced Brass texture of hot-rolled Al-4Cu-1.6Mg alloy by 0.1% Zr addition, Mater. Charact. 169 (2020) 110643.

[29] Q. Zhao, Z.Y. Liu, Y.C. Hu, S.S. Li, S. Bai, Evolution of Goss texture in an Al-Cu-Mg alloy during cold rolling, Arch. Civ. Mech. Eng. 20 (2020) 24.

[30] Q. Zhao, Z.Y. Liu, S. Bai, S.S. Li, Y.C. Hu, P. Xia, Coincidence site lattice boundary mechanism for the preferred growth of Goss and Cube grains during annealing in an Al-Cu-Mg alloy, Mater. Charact. 141 (2018) 193–211.

[31] F. Bachmann, R. Hielscher, H. Schaeben, Texture analysis with MTEX-free and open source software toolbox, Solid State Phenomena 160 (2010) 63–68.

[32] F. Bachmann, R. Hielscher, H. Schaeben, Grain detection from 2d and 3d EBSD data-Specification of the MTEX algorithm, Ultramicroscopy 111 (2011) 1720–1733.

[33] H. Hosseini-Toudeshky, M. Jamalian, Simulation of micromechanical damage to obtain mechanical properties of bimodal Al using XFEM, Mech. Mater. 89 (2015) 229–240.

[34] M. He, F. Li, Z. Wang, Forming limit stress diagram prediction of aluminum alloy 5052 based on GTN model parameters determined by in situ tensile test, Chinese J. Aeronaut. 24 (2011) 378–386.

[35] L. Zhao, P. Chakraborty, M.R. Tonks, I. Szlufarska, On the plastic driving force of grain boundary migration: a fully coupled phase field and crystal plasticity model, Comp. Mater. Sci. 128 (2017) 320–330.

[36] L.P. Evers, D.M. Parks, W.A.M. Brekelmans, M.G.D. Geers, Crystal plasticity model with enhanced hardening by geometrically necessary dislocation accumulation, J. Mech. Phys. Solids 50 (2002) 2403–2424.

[37] H. Sheikh, R. Ebrahimi, E. Bagherpour, Crystal plasticity finite element modeling of crystallographic textures in simple shear extrusion (SSE) process, Mater. Des. 109 (2016) 289–299.

[38] Q. Zhao, Z.Y. Liu, Y.C. Hu, F.D. Li, C. Luo, S.S. Li, Texture effect on fatigue crack propagation in aluminium alloys: an overview, Mater. Sci. Tech. 35 (2019) 1789–1802.

[39] S. Hasunuma, T. Ogawa, Crystal plasticity FEM analysis for variation of surface morphology under low cycle fatigue condition of austenitic stainless steel, Int. J. Fatigue 127 (2019) 488–499.

[40] L. Kubin, B. Devincre, T. Hoc, Modeling dislocation storage rates and mean free paths in face-centered cubic crystals, Acta Mater. 56 (2008) 6040–6049.

[41] A. Ma, F. Roters, A constitutive model for fcc single crystals based on dislocation densities and its application to uniaxial compression of aluminium single crystal, Acta Mater. 52 (2004) 3603–3612.

[42] L. Tabourot, M. Fivel, E. Rauch, Generalised constitutive laws for f.c.c. single crystals, Mater. Sci. Eng. A 234–236 (1997) 639–642.

[43] L. Priester, Grain Boundaries and Crystalline Plasticity, ISTE Ltd., London, 2011.

[44] E. Voce, The relationship between stress and strain for homogeneous deformation, J. Inst. Met. 74 (1948) 537–562.

[45] F. Roters, P. Eisenlohr, L. Hantcherli, D.D. Tjahjanto, T.R. Bieler, D. Raabe, Overview of constitutive laws, kinematics, homogenization and multiscale methods in crystal plasticity finite-element modeling: theory, experiments, applications, Acta Mater. 58 (2010) 1152–1211.

[46] F. Briffod, T. Shiraiwa, M. Enoki, Numerical investigation of the influence of rolling texture and microstructure on fatigue crack initiation in BCC polycrystals, Int. J. Fatigue 107 (2018) 72–82.

[47] L. Li, L.M. Shen, G. Proust, C.K.S. Moy, G. Ranzi, Three-dimensional crystal plasticity finite element simulation of nanoindentation on aluminium alloy 2024, Mater. Sci. Eng. A 579 (2013) 41–49.

[48] P. Efthymiadis, C. Pinna, J.R. Yates, Fatigue crack initiation in AA2024: a coupled micromechanical testing and crystal plasticity study, Fatigue Fract. Eng. Mater. Struct. 42 (2019) 321–338.

[49] P. Efthymiadis, Multiscale Experimentation & Modeling of Fatigue Crack Development in Aluminium Alloy 2024 PhD thesis, University of Sheffield, 2015.

[50] C.T. Luo, Multiscale Modeling & Virtual Sensing for Structural Health Monitoring PhD thesis, Arizona State University, 2011.

[51] N.Q. Chinh, G. Horváth, Z. Horita, T.G. Langdon, A new constitutive relationship for the homogeneous deformation of metals over a wide range of strain, Acta Mater. 52 (2004) 3555–3563.
[52] D.L. Olmsted, S.M. Foiles, E.A. Holm, Survey of computed grain boundary properties in face-centered cubic metals: I. Grain boundary energy, Acta Mater. 57 (2009) 3694–3703.
[53] V. Randle, O. Engler, Introduction to Texture Analysis: Macrotexture, Microtexture, and Orientation Mapping, Gordon and Breach, Amsterdam, Holland, 2000.
[54] W.F. Smith, J. Hashemi, Foundation of Materials Science and Engineering, China Machine Press, Beijing, 2014.
[55] Z.F. Wang, J.J. Zhang, G. Li, Z.W. Xu, H.J. Zhang, J.G. Zhang, A. Hartmaier, F.Z. Fang, Y.D. Yan, T. Sun, Anisotropy-related machining characteristics in ultra-precision diamond cutting of crystalline copper, Nanomanuf. Metrol. 3 (2020) 123–132.
[56] P. Franciosi, L.T. Le, G. Monnet, C. Kahloun, M.-H. Chavanne, Investigation of slip system activity in iron at room temperature by SEM and AFM in-situ tensile and compression tests of iron single crystals, Int. J. Plasticity 65 (2015) 226–249.
[57] Y. Yoshida, J. Shibano, K. Fukuda, K. Terabayashi, M. Eguchi, K. Kajiwara, T. Shobu, A. Shiro, Crystal rotation and microstructures in an aluminum single-slip system under tensile loading, Mater. Charact. 146 (2018) 121–126.
[58] F.H. Shen, D.Q. Yi, Y. Jiang, B. Wang, H.Q. Liu, C. Tang, W.B. Shou, Semi-quantitative evaluation of texture components and fatigue properties in 2524 T3 aluminum alloy sheets, Mater. Sci. Eng. A 657 (2016) 15–25.
[59] X.F. Luan, T. Zhang, C.X. Zhao, Theoretical Mechanics, Harbin Institute of Technology Press, Harbin, 2007.
[60] L. Egghe, L. Leydesdorff, The relation between Pearson's correlation coefficient r and Salton's Cosine measure, J. Am. Soc. Inf. Sci. Tec. 60 (2009) 1027–1036.
[61] C.H. Liu, Deformation Compatibility Behavior of HCP Crystal Structure Alloys at Room Temperature Master thesis, Shanghai Jiao Tong University, 2017.
[62] D.E. Spearot, M.D. Sangid, Insights on slip transmission at grain boundaries from atomistic simulations, Curr. Opin. Solid State Mater. Sci. 18 (2014) 188–195.
[63] W.B. Lee, K.C. Chan, A criterion for the prediction of shear band angles in F.C.C. metals, Acta Metall. Mater. 39 (1991) 411–417.